

# Classical dimers with aligning interactions on the square lattice

Fabien Alet<sup>1,2 \*</sup> Yacine Ikhlef<sup>3,2</sup>, Jesper Lykke Jacobsen<sup>3,2</sup>, Grégoire Misguich<sup>2</sup>, and Vincent Pasquier<sup>2</sup>

<sup>1</sup>Laboratoire de Physique Théorique, UMR CNRS 5152,

Université Paul Sabatier, 31062 Toulouse, France

<sup>2</sup>Service de Physique Théorique, URA CNRS 2306, CEA Saclay, 91191 Gif sur Yvette, France and

<sup>3</sup>LPTMS, UMR CNRS 8626, Université Paris-Sud, 91405 Orsay, France

(Dated: February 6, 2008)

We present a detailed study of a model of close-packed dimers on the square lattice with an interaction between nearest-neighbor dimers. The interaction favors parallel alignment of dimers, resulting in a low-temperature crystalline phase. With large-scale Monte Carlo and Transfer Matrix calculations, we show that the crystal melts through a Kosterlitz-Thouless phase transition to give rise to a high-temperature critical phase, with algebraic decays of correlations functions with exponents that vary continuously with the temperature. We give a theoretical interpretation of these results by mapping the model to a Coulomb gas, whose coupling constant and associated exponents are calculated numerically with high precision. Introducing monomers is a marginal perturbation at the Kosterlitz-Thouless transition and gives rise to another critical line. We study this line numerically, showing that it is in the Ashkin-Teller universality class, and terminates in a tricritical point at finite temperature and monomer fugacity. In the course of this work, we also derive analytic results relevant to the non-interacting case of dimer coverings, including a Bethe Ansatz (at the free fermion point) analysis, a detailed discussion of the effective height model and a free field analysis of height fluctuations.

PACS numbers: 05.20.-y, 05.50.+q, 64.60.Cn, 64.60.Fr, 64.60.Kw

## I. INTRODUCTION

The problem of lattice coverings by "hard" objects, and dimers in particular, is ubiquitous in classical statistical mechanics. The formulation of the problem of dimer coverings goes back to the thirties [1]. The combinatorial problem of finding the exact number of such coverings has been solved in the early sixties for planar 2d lattices by means of Pfaffian techniques [2, 3], which have been extended to calculate dimer-dimer and monomer (*i.e.* unpaired sites)-monomer correlation functions [4]. Notwithstanding the intrinsic mathematical beauty of this problem [5], it also plays a central role in statistical physics due to its relationship to Ising [3] or height models [6]. Dimer coverings of bipartite graphs in three dimensions have also been recently shown to be connected to gauge theories [7]. Dimer models have also recently regained interest because Quantum Dimer Models (QDM), originally introduced by Rokhsar and Kivelson [8], are among the simplest systems which exhibit ground-states with topological order and fractionalization [9].

In this work, we study a model of *interacting* classical dimers on the square lattice, with an interaction that favors dimer alignment. The dimer coverings are close-packed, *i.e.* there are no sites left uncovered by a dimer (monomers). We now describe the plan of the paper: we first introduce the model and its simple limits in Sec. II. In Sec. III we introduce the transfer matrix of the model and describe how its critical exponents in the non-interacting (infinite temperature) limit can be red-

erived by the Bethe Ansatz technique. Unfortunately, the interacting model does not seem to be integrable by a straightforward extension of this approach. We therefore go on, in Sec. IV, to describe two complementary numerical simulation schemes: Monte Carlo (MC) and Transfer Matrix (TM) calculations. The results of the MC simulations are presented in Secs. V, VI and VII: we find that the model possesses a low-temperature crystalline phase separated by a Kosterlitz-Thouless (KT) transition [10] from a high-temperature critical phase with floating exponents. We account for all these findings in Sec. VIII, where we give a theoretical interpretation in terms of a Coulomb gas (CG) picture [11]. This mapping moreover allows use to make specific predictions on the high-temperature phase that are successfully tested with high-precision TM and MC calculations. The CG description implies that the introduction of monomers is a marginal perturbation at the KT point and hence leads to the emergence of another critical line. We study this numerically and find it to be in the Ashkin-Teller universality class; the line terminates in a tricritical point at finite temperature and monomer fugacity. The finally obtained phase diagram is presented in Fig. 1. We finally discuss the connections to other models in classical statistical physics and the implications of our findings for quantum models in Sec. IX, and conclude in Sec. X. A short account of the results presented here was given in Ref. 12.

---

\*Electronic address: alet@irsamc.ups-tlse.fr

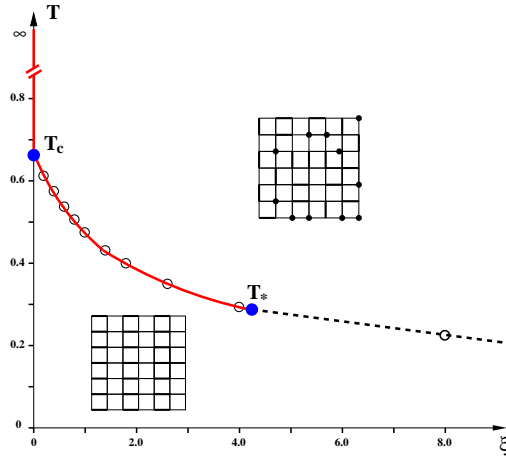


FIG. 1: (Color online) Phase diagram of the interacting dimer model in the temperature  $T$ , monomer fugacity  $\xi$  plane (see text for definitions). The solid lines represent second-order phase transition lines with continuously varying exponents. When no monomers are allowed ( $\xi = 0$ ), the first critical line terminates at  $T_c = 0.65(1)$  and separates the high- $T$  critical phase from a long-range order crystalline phase through a Kosterlitz-Thouless phase transition. Allowing for monomers ( $\xi \neq 0$ ) creates the second critical line separating the low  $T$  crystalline phase from a monomer-dimer (massive) liquid phase at high  $T$ . This line terminates in a multicritical point at  $T_* = 0.29(2)$ , where it changes nature to become a first order line (dashed line). Simple energetic arguments (see Ref. 12) predict that the first order transition temperature scales as  $1/(2 \ln(\xi))$  when  $\xi \rightarrow \infty$ .

## II. THE MODEL

We study a model of interacting close-packed dimers on the square lattice, defined in the following way

$$Z = \sum_c \exp(-E_c/T) \\ E_c = v((N^c(\Xi) + N^c(\Pi)). \quad (1)$$

The sum in the partition function  $Z$  is over all fully-packed dimer coverings of the square lattice  $c$ . To each dimer covering  $c$ , we assign the energy  $E_c$  which simply counts the number  $N^c(\Xi) + N^c(\Pi)$  of plaquettes with parallel (horizontal or vertical) dimers in the covering  $c$ .  $|v| = 1$  sets the energy scale ( $T$  is the temperature). The sign of  $v$  determines the nature of the interactions between the nearest-neighbor dimers :  $v < 0$  correspond to *aligning* interactions between dimers,  $v > 0$  favors configurations with staggered occupation of dimers. In this paper, we will consider  $v = -1$ , the so-called columnar case.

The model is illustrated in Fig. 2, where a dimer covering of the lattice is represented, and the plaquettes contributing a factor  $+v$  to the energy of this configuration

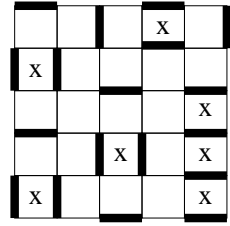


FIG. 2: Illustration of the interacting dimer model : we consider dimer coverings of the square lattice where each plaquette (marked with a cross) with a pair of parallel nearest neighbor dimers contributes  $+v$  to the energy (the energy of this dimer covering is  $7v$ ).

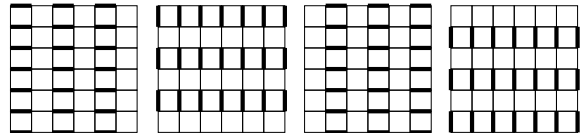


FIG. 3: The four columnar ground states.

are identified by a cross. It is straightforward to see that at zero temperature  $T = 0$ , the configurations that minimize the energy are the four states represented in Fig. 3, where the dimers are aligned in *columns*. This four-fold degenerate ground state spontaneously breaks translation and  $\pi/2$ -rotational symmetries. The first excitation above these ground-states are obtained by flipping two parallel dimers around a plaquette; the system has a gap (it costs a finite energy  $2v$  to flip the two dimers) and the columnar order is therefore expected to subsist at (possibly small but) finite temperature.

On the other hand, the partition function at infinite temperature  $T = \infty$  is simply the unweighted sum over all possible dimer coverings of the square lattice, and the model can be solved exactly at this point [2, 3]. The  $T = \infty$  point is critical, with correlation functions displaying an algebraic dependence with distance [4]: dimer-dimer correlation functions decay as  $1/r^2$  and monomer-monomer correlation functions as  $1/\sqrt{r}$  for large distance  $r$ . We postpone the precise definitions of these correlation functions to Sec. III below where we rederive the results for the critical exponents using another exact approach, the coordinate Bethe Ansatz. Although we have not been able to solve the interacting dimer problem (finite temperature), the Bethe Ansatz technique can potentially go beyond free fermion problems (contrary to the Pfaffian methods of Refs. 2, 3, 4).

The Bethe Ansatz method also serves to illustrate that the critical nature of the dimer covering problem is intimately linked to the bipartite nature of the square lattice (non-bipartite lattices present a dimer liquid behavior with a finite correlation length [9]). Unfortunately, the introduction of interactions appears to break the integrability of the model.

We end up the introduction with some historical notes on this model. The model Eq. (1) was first introduced in the physics of liquid crystals [13] and not developed further in this context to our best knowledge. This is likely due to the fact that the quest was there to look for microscopic models where a true liquid crystal phase exists, and not a crystalline state such as the one depicted in Fig. 3. Later on, Brankov and coworkers [14] also studied the same model with Monte Carlo methods but missed the true critical behavior of this problem. In a recent publication [12] we described the physics of the undoped model and sketched the existence of a critical line with central charge  $c = 1$  ending at a tri-critical point at finite doping. This has then been followed by other studies, including construction of quantum models [15, 16] with ground-state wave-functions described by the partition function in Eq. (1), further investigations of the doped monomer case [15, 16, 17] and generalization to three-dimensional lattices [18].

### III. NON-INTERACTING DIMERS AS FREE FERMIONS

We study dimer coverings (each site is paired with exactly one of its neighbors) of the square lattice. In this section (and only in this section), we give a fugacity  $\omega$  to each horizontal dimer, and 1 to vertical ones. This is the model of *non-interacting* dimers, solved by combinatorial methods [2, 3, 4]. We will introduce the TM of this model and we show how to compute the partition sum and the correlation functions by the Bethe Ansatz method.

#### A. Transfer matrix

The partition sum of the model is:

$$Z = \sum_{\text{dimer config.}} \omega^{\#\text{horizontal dimers}} \quad (2)$$

On a strip of width  $L$ , we define the state of a row as the “occupation numbers”  $\alpha = (\alpha_1, \dots, \alpha_L)$  of the vertical edges, where  $\alpha_i$  is equal to 1 if the  $i$ -th vertical edge is occupied by a dimer, and 0 otherwise. There are  $2^L$  configurations of a row, so  $Z$  can be written as the trace of a  $2^L$ -dimensional transfer matrix  $T$ . We impose periodic boundary conditions (PBC), *i.e.* the index  $i$  is considered modulo  $L$ . Given two line configurations  $\alpha$  and  $\beta$ , the matrix element  $T_{\beta\alpha}$  is the sum of the Boltzmann weights associated with the horizontal dimer configurations  $\mu$  compatible with  $\alpha$  and  $\beta$ :

$$T_{\beta\alpha} = \sum_{\mu|(\alpha, \beta)} \omega^{\mu_1 + \dots + \mu_L} \quad (3)$$

as illustrated in Fig. 4. The compatibility criterion  $\mu|(\alpha, \beta)$  can be expressed formally as follows:

$$\forall i \in \{1, \dots, L\} : \mu_i + \mu_{i+1} + \alpha_i + \beta_{i+1} = 1. \quad (4)$$

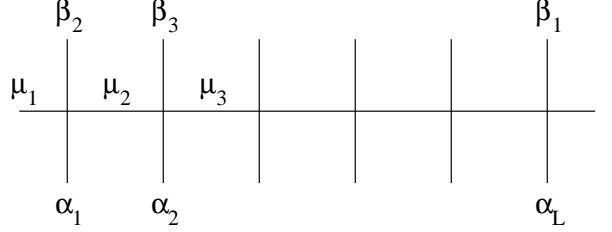


FIG. 4: The row-to-row transfer matrix

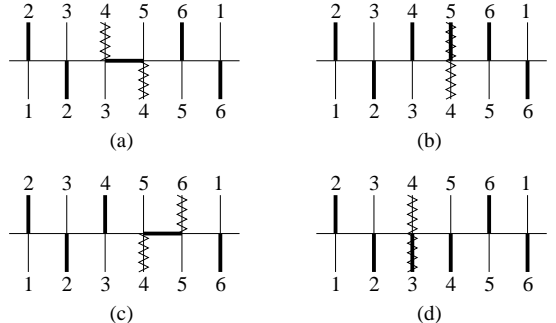


FIG. 5: Rules for the dynamics of the particles on a strip of width  $L = 6$ . Particles are represented by zigzag lines. The rules are different for particles starting from an even site (a, b, c) and an odd site (d).

#### B. Conservation law

For convenience, we introduce a shift at each row in the numbering of columns (see Fig. 4). We call *particle* an empty even vertical edge or an occupied odd vertical edge. Let us show that the number of particles is conserved, and let us give at the same time the rules for the dynamics of the particles (see the corresponding Fig. 5).

*Particle on an even vertical edge:* If a particle sits on the vertical edge  $\alpha_{2j}$ , then  $\alpha_{2j} = 0$ . The site above this edge must be visited once, so one of the variables  $\mu_{2j}$ ,  $\beta_{2j+1}$ ,  $\mu_{2j+1}$  must be equal to 1. In the first (resp. third) case, this implies that  $\beta_{2j}$  (resp.  $\beta_{2j+2}$ ) is zero. Therefore, in the next row, there is a particle on the edge  $\beta_{2j}$ ,  $\beta_{2j+1}$  or  $\beta_{2j+2}$ .

*Particle on an odd vertical edge:* If a particle sits on the vertical edge  $\alpha_{2j-1}$ , then  $\alpha_{2j-1} = 1$ . The site above this edge has already been visited, so  $\beta_{2j}$  must be zero: in the next row, the particle sits on the edge  $\beta_{2j}$ .

The TM is block-diagonal, each block representing a sector with fixed number of particles  $n$ . We call  $T^{(n)}$  the TM block in the  $n$ -particle sector. Note that the lattice width  $L$  must be even, because, for an odd lattice width with PBC, the number of particles is not conserved.

### C. One-particle sector

The action of  $T$  on a one-particle state  $\Phi$  is:

$$\begin{aligned} (T\Phi)_{(2j)} &= \omega\Phi(2j-2) + \Phi(2j-1) + \omega\Phi(2j) \\ (T\Phi)_{(2j+1)} &= \Phi(2j) \end{aligned} \quad (5)$$

We want to take advantage of the translational invariance to diagonalize  $T^{(1)}$ . Define the two-step cyclic permutation  $J$  of the sites by its action on a one-particle state  $\Phi$ :

$$(J\Phi)(x) = \Phi(x+2) \quad (6)$$

On a lattice of even width with PBC, the operator  $J$  commutes with  $T^{(1)}$ . If  $z$  satisfies the condition  $z^L = 1$ , the eigenspace of  $J$  with eigenvalue  $z^2$  is generated by the two vectors  $\Phi_z, \overline{\Phi}_z$ :

$$\begin{aligned} \Phi_z(2j) &= z^{2j}, \quad \Phi_z(2j-1) = 0 \\ \overline{\Phi}_z(2j) &= 0, \quad \overline{\Phi}_z(2j-1) = z^{2j-1} \end{aligned} \quad (7)$$

Note that  $\Phi_{-z} = \Phi_z$  and  $\overline{\Phi}_{-z} = -\overline{\Phi}_z$ .

More generally, let  $z$  be a complex number of modulus unity. The block of  $T^{(1)}$  in the basis  $(\Phi_z, \overline{\Phi}_z)$  is:

$$\begin{bmatrix} \omega(1+z^{-2}) & z^{-1} \\ z^{-1} & 0 \end{bmatrix} \quad (8)$$

This matrix has eigenvectors  $\psi_z, \psi'_z$  with the eigenvalues  $\Lambda(z), \Lambda'(z)$  satisfying:

$$\begin{aligned} \Lambda(z) + \Lambda'(z) &= \omega(1+z^{-2}) \\ \Lambda(z) \Lambda'(z) &= -z^{-2} \end{aligned} \quad (9)$$

One can then write:

$$z = \exp(ik) \quad (10)$$

$$\Lambda(z) = \exp[h + i(\phi + \theta)] \quad (11)$$

$$\Lambda'(z) = \exp[-h + i(\phi - \theta)] \quad (12)$$

where  $k, \phi, \theta$  are real and  $h$  is nonnegative.  $\Lambda(z)$  is the eigenvalue with greatest modulus. With this parametrization, Eqs. (9) imply:

$$\cosh(2h) = 1 + 2\omega^2 \cos^2 k \quad (13)$$

when  $|z| = 1$ . Recalling that  $\cos k \geq 0$ , this relation can be inverted and we obtain:

$$h(k) = \log \left[ \omega \cos k + (1 + \omega^2 \cos^2 k)^{\frac{1}{2}} \right] \quad (14)$$

when  $-\pi/2 \leq k \leq \pi/2$ . A useful quantity for the computation of finite-size effects is  $h'(\pi/2) = -\omega$ .

### D. Two-particle sector, scattering amplitude

Consider the action of the TM on the two-particle vector:

$$\psi_{12}(x_1, x_2) = \psi_{z_1}(x_1)\psi_{z_2}(x_2), \quad x_1 < x_2 \quad (15)$$

The TM changes the positions of the particles from  $(x_1, x_2)$  to  $(y_1, y_2)$ . For fixed positions  $y_1 < y_2$ , let us look at the initial states leading to these positions:

- if  $y_2 > y_1 + 2$  or  $(y_1, y_2) = (2j-1, 2j+1)$ , then for each particle all initial states are allowed, thus:

$$\begin{aligned} (T\psi_{12})(y_1, y_2) &= \sum_{x_1, x_2} \psi_{z_1}(x_1)\psi_{z_2}(x_2) T_{y_1, x_1} T_{y_2, x_2} \\ &= \Lambda(z_1)\Lambda(z_2)\psi_{z_1}(y_1)\psi_{z_2}(y_2) \end{aligned}$$

- if  $(y_1, y_2) = (2j-1, 2j)$ , all initial states are allowed except  $x_1 = x_2 = 2j-2$ . One has to subtract the corresponding term in the action of the matrix  $T$ :

$$(T\psi_{12})(2j-1, 2j) = \Lambda(z_1)\Lambda(z_2)\psi_{z_1}(2j-1)\psi_{z_2}(2j) - \omega\psi_{z_1}(2j-2)\psi_{z_2}(2j-2)$$

- if  $(y_1, y_2) = (2j, 2j+1)$  or  $(y_1, y_2) = (2j, 2j+2)$ , all initial states are allowed except  $x_1 = x_2 = 2j$ . Similarly to the previous case:

$$(T\psi_{12})(2j, 2j+1) = \Lambda(z_1)\Lambda(z_2)\psi_{z_1}(2j)\psi_{z_2}(2j+1) - \omega\psi_{z_1}(2j)\psi_{z_2}(2j)$$

$$(T\psi_{12})(2j, 2j+2) = \Lambda(z_1)\Lambda(z_2)\psi_{z_1}(2j)\psi_{z_2}(2j+2) - \omega\psi_{z_1}(2j)\psi_{z_2}(2j)$$

Note that all the interaction terms in  $T\psi_{12}$  are symmetric functions of the momenta  $k_1, k_2$ . As a consequence, the antisymmetric combination:

$$\psi(x_1, x_2) = \psi_{z_1}(x_1)\psi_{z_2}(x_2) - \psi_{z_2}(x_1)\psi_{z_1}(x_2) \quad (16)$$

is an eigenvector of the matrix  $T$  with eigenvalue  $\Lambda(z_1)\Lambda(z_2)$ .

### E. Periodic boundary conditions, position of the solutions

The analogous construction in the  $n$ -particles sector gives the eigenvectors and eigenvalues:

$$\psi(x_1, \dots, x_n) = \sum_P \epsilon(P) \psi_{z_{p_1}}(x_1) \dots \psi_{z_{p_n}}(x_n) \quad (17)$$

$$\Lambda(z_1, \dots, z_n) = \Lambda(z_1) \dots \Lambda(z_n) \quad (18)$$

where the sum is over all permutations of the integers  $1, \dots, n$  and  $\epsilon(P)$  is the signature of the permutation  $P$ . PBC yield:

$$\forall j \quad (z_j)^L = (-1)^{n-1} \quad (19)$$

The solutions of these equations lie on the unit circle, which justifies the discussion in section III C. The momenta  $k_j$  are given by:

$$\begin{aligned} k_j &= \frac{2\pi}{L} I_j, & I_j \in \mathbb{Z} & n \text{ odd} \\ k_j &= \frac{2\pi}{L} (I_j + \frac{1}{2}), & I_j \in \mathbb{Z} & n \text{ even} \end{aligned} \quad (20)$$

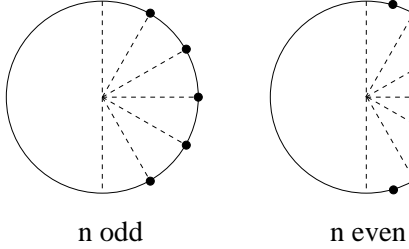


FIG. 6: Position of the vacancies for a strip of width  $L = 12$ . Vacancies are represented by black points on the unit circle, in the complex  $z$  plane.

See Fig. 6 for a graphical representation of the vacancies on the unit circle. For any  $z$  on the unit circle, the TM has an eigenvalue  $\Lambda$  with modulus greater than one. Therefore, the number of particles that maximizes the total eigenvalue of  $T$  is either the greatest even value or the greatest odd value for  $n$ . Since the  $k_j$ 's are distinct, lie in the interval  $[-\pi/2, \pi/2]$  and are spaced by  $2\pi/L$ , the maximum number of particles is  $L/2$ .

#### F. Thermodynamic limit

In this section, the discussion is restricted for simplicity to a system of width multiple of four:  $L = 4p$ . According to the previous section, the leading sector is defined by the greatest eigenvalue either in the sector  $n = 2p$  or in the sector  $n = 2p - 1$ . As will be shown in a few lines, the correct choice for the leading sector is  $n = 2p$ .

For a system of finite width and infinite length, the free energy density per surface unit in the  $n$ -particles sector is defined by:

$$f_L^{(n)} = \frac{1}{L} \log \Lambda_{\max}^{(n)} \quad (21)$$

where  $\Lambda_{\max}^{(n)}$  is the eigenvalue of  $T$  with greatest modulus in the  $n$ -particles sector. The corresponding quantity for  $L = 4p$  and  $n = 2p$  is:

$$f_L^{(L/2)} = \frac{2}{L} \sum_{j=0}^{p-1} h \left[ (j + 1/2) \frac{2\pi}{L} \right] \quad (22)$$

where the function  $h(k)$  is given by Eq. (14). When  $L$  goes to infinity, this quantity tends to the limit  $f_\infty$ :

$$f_\infty = \frac{1}{\pi} \int_0^{\frac{\pi}{2}} \log \left[ \omega \cos k + (1 + \omega^2 \cos^2 k)^{\frac{1}{2}} \right] dk \quad (23)$$

in agreement with formula (17) of Ref. 2. In the isotropic case  $\omega = 1$ :

$$f_\infty(\omega = 1) = \frac{2G}{\pi} \quad (24)$$

where  $G$  is the Catalan constant:

$$G = 1^{-2} - 3^{-2} + 5^{-2} - 7^{-2} + \dots \quad (25)$$

The asymptotic behavior of  $f_L^{(L/2)}$  is derived from the Euler-Maclaurin formula:

$$f_L^{(L/2)} = f_\infty + \omega \frac{\pi}{6L^2} + o(L^{-2}). \quad (26)$$

We expect the critical point to have conformal symmetry in the isotropic case, with a central charge  $c = 1$ . If one particle is removed ( $n = 2p - 1$ ), the solutions  $z_j$  all get shifted (see Fig. 6). The Euler-Maclaurin formula yields:

$$f_L^{(L/2-1)} = f_\infty - \frac{\pi}{6L^2} h' \left( \frac{\pi}{2} \right) - \frac{1}{\pi} I(\pi/L) + o(L^{-2}) \quad (27)$$

with

$$I(\epsilon) = \int_{\frac{\pi}{2}-\epsilon}^{\frac{\pi}{2}} h(k) dk = -h' \left( \frac{\pi}{2} \right) \epsilon^2/2 + o(\epsilon^2). \quad (28)$$

Finally we obtain:

$$f_L^{(L/2-1)} = f_L^{(L/2)} - \frac{\pi}{2L^2} \omega + o(L^{-2}) \quad (29)$$

This proves that in the thermodynamic limit the leading sector is indeed given by  $n = 2p$ . In the isotropic case, the critical exponent corresponding to the removal of one particle is  $X_1 = 1/4$  (see definition and discussion in Sec. IV B below). Now if two particles are removed from the leading sector, the other  $z_j$ 's are not shifted, because the number of particles remains even. The only effect is a decrease of free energy caused by the absence of the two particles:

$$f_L^{(L/2-2)} = f_L^{(L/2)} - \frac{2}{L} h \left( \frac{\pi}{2} - \frac{\pi}{L} \right) \quad (30)$$

$$= f_L^{(L/2)} - \frac{2\pi}{L^2} \omega + o(L^{-2}) \quad (31)$$

In the isotropic case, the critical exponent corresponding to this process (see again Sec. IV B below) is  $X_2 = 1$ .

#### G. Introducing interactions

A TM for the interacting model Eq. (1) can be written down by generalizing the working of Sec. III A. To this end, the basis states  $(\alpha)$  must encode not only the occupation numbers of a row of vertical edges (as before), but also the occupation numbers of the preceding row of horizontal edges, as shown in Fig. 7.

The transfer matrix  $T$  is most easily defined by giving its sparse matrix decomposition

$$T = T_2 T_1, \quad T_k = \prod_{i=0}^{L-1} T_k^{(i)}, \quad (32)$$

where the matrix  $T_1^{(i)}$  encodes the interactions at plaquette  $i$  and  $T_2^{(i)}$  imposes the dimer constraint at vertex

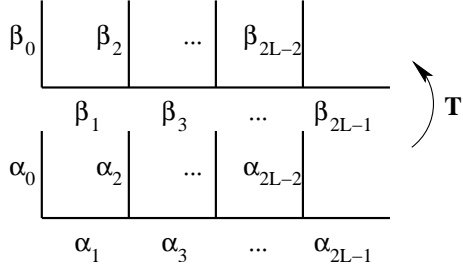


FIG. 7: The row-to-row transfer matrix for the interacting case.

i. More precisely,  $T_1^{(i)}$  evolves  $\alpha_{2i+1}$  into  $\beta_{2i+1}$  and has matrix elements (we set  $W \equiv e^{-v/T}$ )

$$T_1^{(i)}(\alpha_{2i}\alpha_{2i+1}|\beta_{2i+1}\alpha_{2i+2}) = W(\alpha_{2i}\alpha_{2i+2} + \alpha_{2i+1}\beta_{2i+1}),$$

whereas  $T_2^{(i)}$  evolves  $\alpha_{2i}$  into  $\beta_{2i}$  and has matrix elements

$$T_2^{(i)}(\beta_{2i-1}\alpha_{2i}|\beta_{2i}\beta_{2i+1}) = \delta_{\beta_{2i-1}+\alpha_{2i}+\beta_{2i}+\beta_{2i+1}, 1}.$$

We have attempted to diagonalize  $T$  using the Bethe Ansatz method, using a straightforward generalization of the working exposed in the preceding subsections but we failed to obtain a consistent determination of the scattering amplitudes  $S(z_i, z_j)$ . Most likely, this means that the interacting dimer model is not integrable. In the remainder of the paper, we therefore study the model using numerical and (non-rigorous) field theoretical methods.

#### IV. NUMERICAL METHODS

Our numerical methods consist in MC simulations and exact diagonalization of the TM. We now describe these two methods in turn.

##### A. Monte Carlo calculations

We use a MC directed-loop (or directed-“worm”) algorithm [19]. This method allows to make non-local moves in the dimer configurations by changing the positions of dimers along a closed loop, which can be quite large. This results in small autocorrelation times in the MC process, and permits to treat large systems (up to  $512 \times 512$  in this study). Moreover, the directed-loop algorithm captures the physics of test defects (monomers) in the dimer configuration as we discuss below. The algorithm indeed allows to calculate monomer-monomer correlation function; conversely, this indicates that the performance of the algorithm is dictated by the physical properties of test monomers in the different physical phases.

For sake of completeness, we briefly describe below the algorithm following Ref. 19 and specifying minor details where our specific implementation differs. One MC sweep of the algorithm consists of the three following steps:

1. The worm, which can be seen as constituted by two monomers (head and tail), is initially placed on top of a dimer configuration at a random site  $i = i_0$ .
2. The site  $i$  is connected to a neighboring site  $j$  by a dimer in the background configuration (this dimer is noted  $(i, j)$ ). The head of the worm is moved to  $j$  and the dimer  $(i, j)$  is removed, leaving the site  $j$  with no dimer attached to it. Out of the four neighbors of  $j$ , one (which we call  $k$ ) is selected according to a local detailed balance rule (see below). A dimer is put between  $j$  and  $k$ .
3. If  $k = i_0$ , the worm is finished and we are left with a new valid dimer configuration. Otherwise, we rename  $i = k$  and go back to step 2.

How does the worm, sitting at site  $j$  (and coming from site  $i$ ), choose the site  $k$  where a dimer will be put in step 2? For this, we consider the weights  $w_{(ij)}$  (respectively  $w_{(jk)}$ ) contributed to the partition function by a dimer located between sites  $i$  and  $j$  (respectively  $j$  and  $k$ ). In the model of Ref. 19, each dimer is given a certain fugacity and thus contributes solely a certain weight to the partition function. In our model, the weight of a dimer  $(i, j)$  is given by  $w_{(ij)} = \exp(-v.N_{ij}/T)$  where  $N_{ij} \in \{0, 1, 2\}$  is the number of nearest neighbors parallel to the dimer  $(i, j)$ . Once these weights are known, the probability  $P((i, j) \rightarrow (j, k))$  to select a given site  $k$  is imposed to satisfy a local detailed balance rule:

$$P((i, j) \rightarrow (j, k))w_{(ij)} = P((j, k) \rightarrow (i, j))w_{(jk)}. \quad (33)$$

This leads to a set of equations (“directed-loop” equations [19]) corresponding to all the possible values of local dimer configurations and the corresponding numbers  $N_{ij}$ . These equations are underdetermined, and we impose by experience [20, 21] to minimize the bounce processes  $P((i, j) \rightarrow (j, i))$ , *i.e.* the case where the site  $k$  is chosen to be the origin site  $i$  (the worm backtracks in its own path, which is *a priori* quite useless). For the specific model of Ref. 19, a solution minimizing the bounce probabilities and satisfying the local detailed balance equation was found analytically. More generally, such a solution can always be found numerically with linear programming techniques [21]. Please note that at  $T = \infty$ , the worm simply performs a random walk in the dimer configuration (more precisely, all the even steps in the walk are purely random, the odd ones are dictated by the underlying dimer configuration).

Taking a snapshot of the configuration during the worm construction shows that two test monomers have been inserted in the dimer configuration, and thus connect the behavior of the worm to the monomer correlation function. The fact that the worm walk is *locally* detailed balance actually imposes the histogram of the distance  $\mathbf{r}$  between the worm’s head and tail to be proportional (up to a small correction factor) to the monomer-monomer correlation function  $M(\mathbf{r})$  (see precise definition in Sec. VII). The proof of this statement can be

worked out along the lines of Ref. 21. The only subtlety is the following: the measurement of the correlation function is made at step 2, before the selection of the next site  $k$ . Since all the future dimer positions  $(j, k)$  are not equivalent (they will contribute differently to the partition function) and since the next dimer position is not yet decided, we have to correct the monomer-monomer correlation estimator by the inverse of the total weight contributed by all possible future positions, *i.e.* we increment the estimator of  $M(\mathbf{r})$  (with  $\mathbf{r}$  the position difference vector between sites  $i_0$  and  $j$ ) by  $W_j^{-1}$  where  $W_j = \sum_k w_{(jk)}$ . If all future position dimers are equivalent (as in the model of Ref. 19), this factor is constant, and we can just simply identify the histogram of the distance  $\mathbf{r}$  between the worm's head and tail to  $M(\mathbf{r})$ .

The worm algorithm therefore possesses the nice feature of being able to calculate  $M(\mathbf{r})$ , *even if monomers are not allowed in the model*. This also indicates that the worm algorithm performances is bound to follow the physics of monomers: if the monomers are confined, the worms will be short, resulting in a merely local algorithm - which is known to display poor performances (for example ergodicity problems). If the monomers are deconfined, worms will be long and will update a massive number of dimers - resulting in small autocorrelation times.

The technical details of the MC calculations are as follows: simulations were performed on  $N = L \times L$  samples, up to  $L = 160$  for the full  $T$  range, and up to  $L = 512$  for correlation functions for a few chosen temperatures. PBC are assumed. Each MC sweep is constituted by a number of worms such that all the links of the lattice are visited once on average by a worm. For each parameter set, a total between  $10^6$  and  $10^7$  sweeps was performed.

## B. Transfer matrix calculations

The TM for the interacting dimer model was defined above in Sec. III G. We shall henceforth suppose that the width  $L$  of the lattice strip is even; the periodic boundary conditions in the  $L$ -direction are then compatible with the bipartiteness of the lattice. By virtue of the conservation law established in Sec. III B, the TM has a block diagonal structure, with each block corresponding to a fixed number of particles. It is convenient to define a “charge”  $Q$  corresponding to each block, as  $Q = L/2 - n$ , where  $n$  is the number of particles. Also, we label the eigenvalues  $\Lambda_k^Q$  within each block in order of decreasing norm:  $|\Lambda_1^Q| \geq |\lambda_2^Q| \geq \dots$

### 1. Correlation functions

For entropic reasons, the largest eigenvalue must be located in the  $Q = 0$  block,  $\Lambda_{\max} = \Lambda_1^0$ . By the Perron-Frobenius theorem, it corresponds to the unique eigenvector in which all entries are non-negative. Consider first a dimer covering of a strip of size  $L \times M$ , with free

(resp. periodic) boundary conditions in the  $M$  (resp.  $L$ ) direction. Only the TM eigenvalues of the  $Q = 0$  block will contribute to the corresponding partition function  $Z$ . Let us now modify the problem by marking  $Q_0 > 0$  vertices of the even sublattice in the bottom row, and  $Q_0$  vertices of the odd sublattice in the top row. In the modified problem, dimers are required to cover all unmarked vertices and none of the marked vertices. The TM eigenvalues contributing to the modified partition function  $Z_{Q_0}$  are then exactly those of the  $Q = Q_0$  block. (For  $Q_0 < 0$ , interchange the two sublattices and change the sign of  $Q_0$ ).

Physically, the marked vertices can be interpreted as monomer defects in the surrounding dimer environment. The ratios  $C_{Q_0}(M) \equiv Z_{Q_0}/Z$  define (unnormalized) correlation functions, measuring the correlations between the two groups of monomers, separated by a distance  $M$ . For  $M \gg L$  the correlations decay exponentially as  $C_{Q_0}(M) \sim (\lambda_1^{Q_0}/\Lambda_1^0)^M$ .

If the system enjoys conformal invariance, this corresponds to an algebraic decay in the plane. More precisely, define the free energies per unit area as  $f_k^Q = L^{-1} \log \Lambda_k^Q$ . The finite-size dependence [22]

$$f_1^0 - f_1^{Q_0} = \frac{2\pi X_{Q_0}}{L^2} + o(L^{-2}) \quad (34)$$

then defines a critical exponent  $X_{Q_0}$  whose interpretation reads as follows: let  $\mathcal{C}_N$  be a dimer covering of an  $N \times N$  square with free boundary conditions (planar geometry), with two small regions of  $Q_0$  monomer defects, each region corresponding to a definite sublattice as above. Suppose that each region has an extent of the order of the lattice spacing and is far from the boundaries. Then the probability that the two regions are separated by a distance  $r$  satisfying  $1 \ll r \ll N$  is proportional to  $r^{-2X_{Q_0}}$ .

The corresponding conformal field theory (CFT) is further characterized by its central charge  $c$ , which is related to the finite-size dependence of  $\Lambda_{\max}$  as follows [23]:

$$f_1^0 = f_\infty + \frac{\pi c}{6L^2} + o(L^{-2}), \quad (35)$$

where  $f_\infty = \lim_{L \rightarrow \infty} f_1^0$  is the bulk free energy.

While  $X_1$  determines the leading monomer-monomer correlation function, the leading dimer-dimer correlation can be obtained from Eq. (34) by replacing  $f_1^{Q_0}$  by  $f_2^0$ .

### 2. Numerical procedure

The leading eigenvalue of a given block  $Q$  is obtained by an iterative procedure (the so-called power method [24]) in which the relevant TM block  $T_Q$  is multiplied onto a vector of weights which is indexed by the basis states of that block. This vector can be taken initially as a single arbitrary basis state, which is known to belong to the block  $Q$ . The eigenvalue  $\Lambda_1^Q$  is then related to the asymptotic growth of the norm of the iterated vector.

$L$	2	4	6	8	10	12	14	16	18
$\dim(T_0)$	4	16	76	384	2004	10672	57628	314368	1728292
$\dim(T_1)$	1	8	48	272	1520	8472	47264	264224	1480608
$\dim(T_2)$		1	12	96	660	4224	26012	156608	929700
$\dim(T_3)$			1	16	160	1304	9520	65056	426000
$\dim(T_4)$				1	20	240	2268	18688	141156

TABLE I: Dimensions of the various blocks  $T_Q$  of the transfer matrix, as functions of the strip width  $L$ .

This procedure has multiple practical advantages: (i) only the iterated vector, and not  $T_Q$  itself, needs to be stored in memory, (ii) using the factorization Eq. (32) one can take advantage of sparse matrix techniques, so that one iteration is performed in time  $\sim L \cdot \dim(T_Q)$ , (iii) the complete state space corresponding to  $T_Q$  is automatically generated in the iterative process. To store and access the weights in an efficient manner (*i.e.* in constant time), standard hashing techniques are employed.

To obtain higher eigenvalues,  $\Lambda_k^Q$  with  $k \geq 2$ , one can similarly iterate a set of vectors which is kept mutually orthogonal at the end of each iteration [24]. Alternatively, one can in some cases use the symmetry of the corresponding eigenvectors. As an example of this, note that the eigenvectors corresponding to  $\Lambda_1^0$  (resp.  $\Lambda_2^0$ ) are even (resp. odd) upon shifting the lattice by one unit in the horizontal direction.

The computational effort needed to obtain the largest eigenvalue can be judged from Table I which shows the size of the block  $T_0$  for various strip widths  $L$ . Note that these numbers increase much slower than the naive estimate  $4^L$ , that one would obtain by considering the possible occupation numbers while ignoring the dimer constraint and the value of  $Q$ . We limited the present study to  $L_{\max} = 18$ , although a couple of more sizes could have easily been obtained.

The values of  $\dim(T_Q)$  can easily be obtained analytically using generating function techniques. The result is that  $\dim(T_Q)$  for a given (even) value of  $L$  is the coefficient in the term  $q^Q$  in the polynomial expansion of

$$\left( \frac{1+4q+q^2+(1+q)\sqrt{1+6q+q^2}}{2q} \right)^{L/2} + \left( \frac{1+4q+q^2-(1+q)\sqrt{1+6q+q^2}}{2q} \right)^{L/2}. \quad (36)$$

The dimension  $\dim(T) = \sum_{Q=-L/2}^{L/2} \dim(T_Q)$  of the total TM is then simply

$$\dim(T) = (1 + \sqrt{2})^L + (1 - \sqrt{2})^L. \quad (37)$$

This is also the dimension of the (unique block of the) TM when monomers are allowed; see Sec. VIII B 3 below.

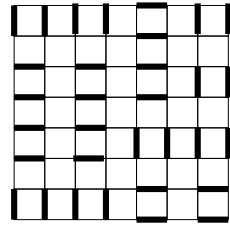


FIG. 8: A typical plaquette configuration.

## V. COLUMNAR ORDER AT LOW TEMPERATURE

### A. Possible crystalline orderings

We present here MC results concerning the nature of the low- $T$  phase. From the energy form, we expect at low- $T$  a proliferation of plaquettes containing parallel dimers. A natural expectation is to have a single low- $T$  phase breaking the same symmetries as the ground-states in Fig. 3: we refer to such an order breaking both translation and  $\pi/2$  rotation symmetries as *columnar order*. On the other hand, from our knowledge of QDM, we know that another type of order could also be stabilized: *plaquette order*. We describe more precisely this order below. As to discriminate which kind(s) of phase(s) is (are) found at low- $T$  in the dimer model Eq. (1), we will introduce three different order parameters.

#### 1. Description of plaquette ordering

The QDM on the square lattice is believed to have some *plaquette* long-ranged order in some finite region of parameter space at  $T = 0$ . In such a symmetry broken phase, one quarter of the square plaquettes are spontaneously selected to host a pair of (quantum-mechanically) resonating dimers. The resulting state breaks translation invariance but is invariant under  $\pi/2$  rotation with respect to the center of any plaquette (see Ref. 25 for an illustration). In the quantum system, a plaquette phase has a (slightly) higher potential energy than a columnar crystal, but the stronger dimer *resonances* lower the plaquette state energy through the *kinetic* terms of the quantum Hamiltonian. Of course, in our classical model, kinetic terms are absent. Still, the *thermal* fluctuations of the dimer locations around each “flippable” plaquette allow to gain some *entropy* (compared to that of a columnar crystal) and lower the free energy. The competition between entropy and potential energy in the classical system is analogous to that between kinetic and potential terms in the QDM. As the plaquette phase is likely to be realized at  $T = 0$  in the QDM, it is *a priori* also a natural candidate in the (finite temperature) phase diagram of the classical model.

In a plaquette phase, two distant flippable plaquettes

are almost uncorrelated: if the first one is dimerized, say, horizontally, the second can be found in both states with equal probability (hence the  $\pi/2$  rotation symmetry). This is not true for nearby - and necessarily correlated - plaquettes, thus defining some finite correlation length. A columnar state can be viewed as a plaquette phase in which this plaquette-plaquette correlation length has grown to infinity so that all the plaquettes of the lattice simultaneously adopt the same orientation. A typical plaquette configuration is displayed in Fig. 8. The plaquette phase breaks translational symmetry but not  $\pi/2$ -rotational symmetry. A possible scenario (eventually ruled out by the numerical results, see below) could therefore be melting of the columnar crystal through an intermediate plaquette phase with partial restoration of the rotation symmetry.

## 2. Order parameters

*Complex columnar order parameter* — We first use the definition (proposed in Ref. 26) of a complex columnar order parameter  $\Psi_{\text{col}}(\mathbf{r})$  at site  $\mathbf{r}$

$$\begin{aligned} \Psi_{\text{col}}(\mathbf{r}) = & (-)^{r_x} [\hat{n}(\mathbf{r} + \mathbf{x}/2) - \hat{n}(\mathbf{r} - \mathbf{x}/2)] \\ & + i (-)^{r_y} [\hat{n}(\mathbf{r} + \mathbf{y}/2) - \hat{n}(\mathbf{r} - \mathbf{y}/2)], \end{aligned} \quad (38)$$

where  $\mathbf{x}, \mathbf{y}$  are unit vectors, and  $\hat{n}$  is the dimer bond occupation number (*i.e.*  $\hat{n}(\mathbf{r} + \mathbf{x}/2)$  is 1 if there's a dimer between site  $\mathbf{r}$  and site  $\mathbf{r} + \mathbf{x}$ ). We define the associated columnar susceptibility as

$$\chi_{\text{col}} = \frac{4}{L^2} (\langle |\sum_{\mathbf{r} \in A} \Psi_{\text{col}}(\mathbf{r})|^2 \rangle - \langle |\sum_{\mathbf{r} \in A} \Psi_{\text{col}}(\mathbf{r})| \rangle^2), \quad (39)$$

where the sums are taken only over the sublattice A. Another interesting quantity is the columnar Binder [27] cumulant

$$B_{\text{col}} = 1 - \frac{\langle |\Psi|^4 \rangle}{2 \langle |\Psi|^2 \rangle^2}. \quad (40)$$

This Binder cumulant saturates to 1/2 for a long-range ordered phase, and scales to 0 in the thermodynamic limit for a phase with no long-range order, due to the Gaussian nature of the fluctuations of this order parameter. As was already noted in Ref. 25, this order parameter (and associated quantities) is sensitive to translation symmetry breaking and a non-zero expectation value detects both columnar and plaquette ordering. Looking at the *phase* of  $\Psi_{\text{col}}$  can in principle discriminate between the two phases: however the phase turns out to be a noisy observable in our simulations and has no practical use. We will therefore use other indicators.

*Dimer rotation symmetry breaking* — At sufficiently high temperatures, the system is symmetric under  $\pi/2$  rotations so that the average number of vertical dimers is equal to the average number of horizontal ones. This

also holds in a plaquette phase, but is no longer true for a columnar state. A convenient way of monitoring the  $\pi/2$ -rotation symmetry [25] is the Dimer Symmetry Breaking:

$$D = 2/L^2 |N^c(\mathbf{-}) - N^c(\mathbf{I})| \quad (41)$$

where  $N^c(\mathbf{-})$  (resp.  $N^c(\mathbf{I})$ ) is the number of horizontal (resp. vertical) dimers in the configuration  $c$ . Normalization is such that  $D = 1$  in the pure columnar states of Fig. 3. It is also useful to define the corresponding susceptibility  $\chi_D = L^2(\langle D^2 \rangle - \langle D \rangle^2)$  and Binder cumulant  $B_D = 1 - \langle D^4 \rangle / (3 \langle D^2 \rangle^2)$ .

*Plaquette order parameter* — To discriminate *positively* the plaquette phase, we also use the following plaquette order parameter

$$P = 2/L^2 \left| \sum_{\mathbf{p}} (-)^{p_x+p_y} v_{\mathbf{p}} \right| \quad (42)$$

where the sum is over all *plaquettes* of the lattice with coordinates  $\mathbf{p} = (p_x, p_y)$ , and  $v_{\mathbf{p}} = 1$  if the plaquette with coordinates  $\mathbf{p}$  contains two parallel dimers ( $v_{\mathbf{p}} = 0$  otherwise). This quantity can also be seen as a generalized energy at wave vector  $(\pi, \pi)$ . The staggered factor  $(-)^{p_x+p_y}$  is essentially constant in a pure plaquette state, and makes the sum vanish in a columnar state. The expectation value  $\langle P \rangle$  of the plaquette order parameter is then 0 in the columnar phase, and saturates to a finite value in the thermodynamic limit in a plaquette phase. The associated plaquette susceptibility is  $\chi_P = L^2(\langle P^2 \rangle - \langle P \rangle^2)$  and plaquette Binder cumulant  $B_P = 1 - \langle P^4 \rangle / (3 \langle P^2 \rangle^2)$ .

## B. Numerical results

### 1. Dimer rotation symmetry breaking

The expectation value  $\langle D \rangle$  is displayed versus  $T$  in Fig. 9 and clearly saturates to its maximum values at low  $T$ . The curves for different system sizes start to differ at a temperature around  $T \sim 0.6$  and in order to detect more finely the critical temperature  $T_c$ , we use the corresponding susceptibility  $\chi_D$  and Binder cumulant  $B_D$ .

$\chi_D$  shows a pronounced peak around  $T \sim 0.63$  (see Fig. 10), signaling the onset of long-range order. Noticing that the temperature at which the susceptibility peaks slightly drifts when increasing system size, we differ an estimation of  $T_c$  in favor of the Binder cumulant, which is known to allow accurate determinations of  $T_c$ .

The Binder cumulant  $B_D$  saturates in the thermodynamic limit to 2/3 at low  $T$  (see Fig. 11) and we observe a crossing of the curves for different system sizes for both cumulants at a unique temperature  $T_c$ , signaling the entrance into the low  $T$  columnar phase. The critical temperature is estimated from this curve to be  $T_c = 0.65(1)$ .

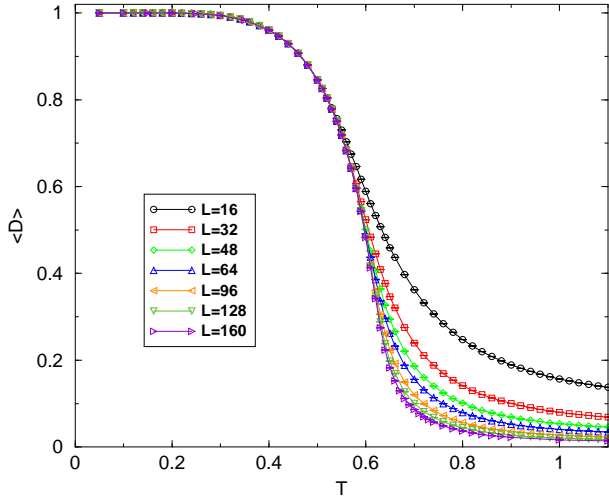


FIG. 9: (Color online) Dimer symmetry breaking order parameter  $\langle D \rangle$  versus temperature  $T$  for different system sizes.

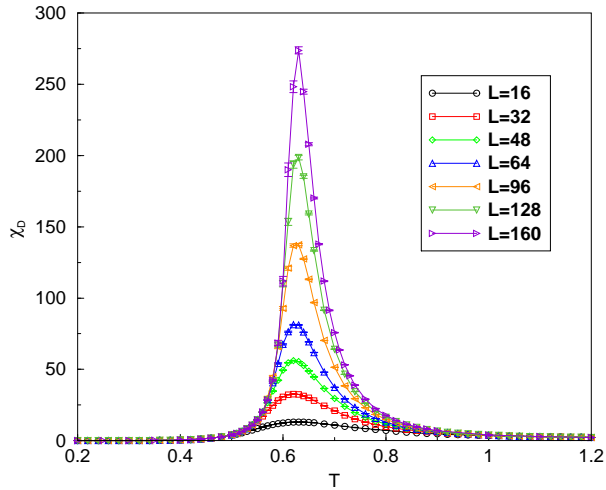


FIG. 10: (Color online) Dimer symmetry breaking susceptibility  $\chi_D$  versus temperature  $T$  for different system sizes.

The results of this section also indicate that plaquette order is not present below  $T_c$ , but leave open the possibility of a plaquette phase at higher  $T$ .

## 2. Plaquette correlations

The expectation value of the plaquette order parameter  $\langle P \rangle$  shows a non-monotonous behavior as a function of  $T$  (see Fig. 12), with an order parameter peaking close to  $T_c \sim 0.65$  from above for all system sizes. One also immediately notes that  $\langle P \rangle$  has overall small values and *decreases* with system size. The plaquette susceptibility  $\chi_P$  peaks slightly above  $T_c$  (see Fig. 13): we interpret this as

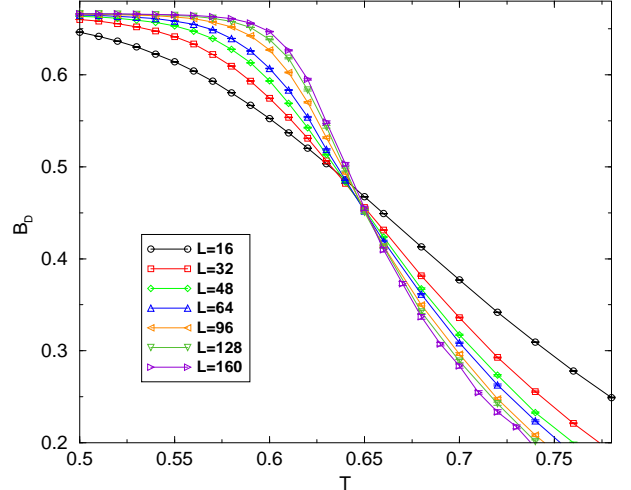


FIG. 11: (Color online) Dimer symmetry breaking Binder cumulant  $B_D$  versus temperature  $T$  for different system sizes.

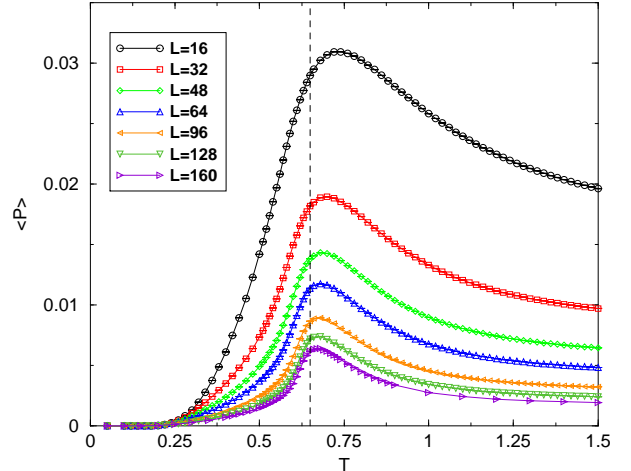


FIG. 12: (Color online) Plaquette order parameter  $\langle P \rangle$  versus temperature  $T$  for different system sizes. The dashed line denotes  $T_c = 0.65(1)$  as estimated by the Dimer symmetry breaking cumulant.

plaquette correlations being the strongest just before the entrance into the columnar phase. Even though the  $\chi_P$  values are very small values as compared to other typical susceptibilities (see for example Fig. 10), long-range plaquette order could survive in the thermodynamic limit. This is clearly ruled out by the behaviour of the plaquette Binder cumulant (see Fig. 14) which is non-monotonous as well:  $B_P$  starts to rise from its high- $T$  zero value when decreasing temperature and suddenly drops down to zero at a temperature slightly above  $T_c$ . This excludes long-range plaquette order.

We conclude that (strong) plaquette correlations are present, start to develop as one decreases  $T$ , peak just

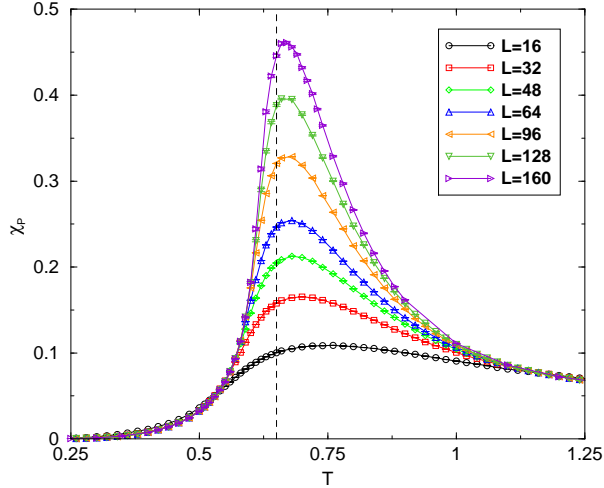


FIG. 13: (Color online) Plaquette susceptibility  $\chi_P$  versus temperature  $T$  for different system sizes. The dashed line denotes  $T_c = 0.65(1)$ .

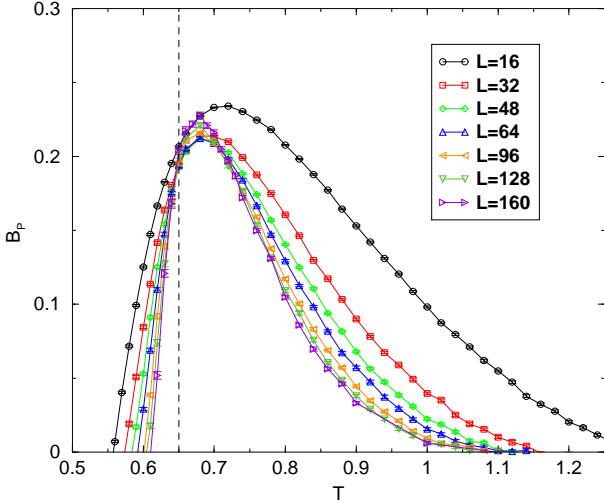


FIG. 14: (Color online) Plaquette Binder cumulant  $B_P$  versus temperature  $T$  for different system sizes. The dashed line denotes  $T_c = 0.65(1)$ .

above  $T_c$ , but do not form a true thermodynamic phase as they are suddenly overtaken by columnar order. However, as we show in the next section, these correlations possibly ‘‘pollute’’ the finite-size behavior of the complex columnar order parameter.

### 3. Complex columnar order parameter

The columnar order parameter  $\langle |\Psi_{\text{col}}| \rangle = \frac{2}{L^2} \langle |\sum_{\mathbf{r} \in A} \Psi_{\text{col}}(\mathbf{r})| \rangle$  is displayed in Fig. 15 for different system sizes (from  $L = 16$  to  $L = 160$ ). One

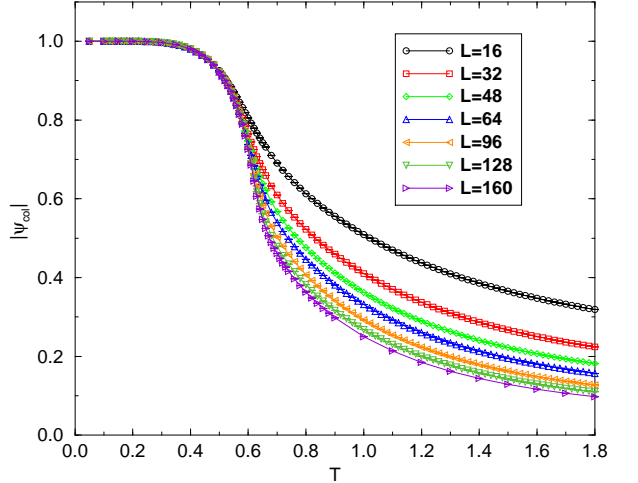


FIG. 15: (Color online) Columnar order parameter  $\langle |\Psi_{\text{col}}| \rangle$  as a function of temperature  $T$  for different system sizes.

clearly sees order setting in at low  $T$ , and the curves for different  $L$  start to separate roughly around  $T \sim 0.6$ . To determine more precisely the critical point, we inspect the behavior of the columnar susceptibility (Eq. (39) and Fig. 16) and Binder cumulant (Eq. (40) and Fig. 17).

The columnar susceptibility has an unexpected behavior. It exhibits two peaks: the first is quite sharp and localized around  $T \sim 0.63$ , and the second is much broader around  $T \sim 1$ . It is also to be noted that whereas for small system sizes ( $L \leq 96$ ), the first peak is smaller than the second one, the tendency is inverted for the two largest system sizes. This could mean that the second peak actually saturates to a finite value in the thermodynamic limit. Another possible scenario is that the two peaks merge, which is not unlikely noticing that the positions of the maximum of the second peaks shift toward lower  $T$  when increasing  $L$ . Unfortunately, the currently available system sizes do not allow us to draw definitive conclusions on the scaling behaviour of  $\chi_{\text{col}}$ .

The columnar Binder cumulant (Fig. 17) also displays unusual features: a very flat pseudo-crossing of the curves for different  $L$  is observed around  $T \sim 1.8$  (see zoom on left inset of Fig. 17) and a marked anomaly around  $T \sim 0.63$  (see zoom on right inset). A crossing of curves corresponding to different system sizes for a Binder cumulant usually denotes a transition to a long-range ordered phase. However, the crossing observed here is very flat and it is actually almost impossible within the statistical accuracy to locate a single crossing point for the three largest samples. The anomaly around  $T \sim 0.63$  is particularly singular and we are not aware of such a behavior being reported for a Binder cumulant in the literature. The fact that two singularities are observed both in  $\chi_{\text{col}}$  and  $B_{\text{col}}$  could be interpreted at first glance as signs of an intermediate phase. However, given our previous findings of strong but no long-range ordered plaquette

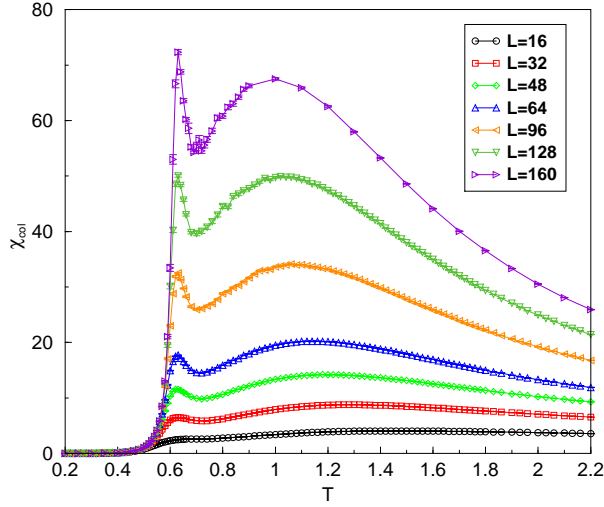


FIG. 16: (Color online) Columnar susceptibility  $\chi_{\text{col}}$  as a function of temperature  $T$  for different system sizes.

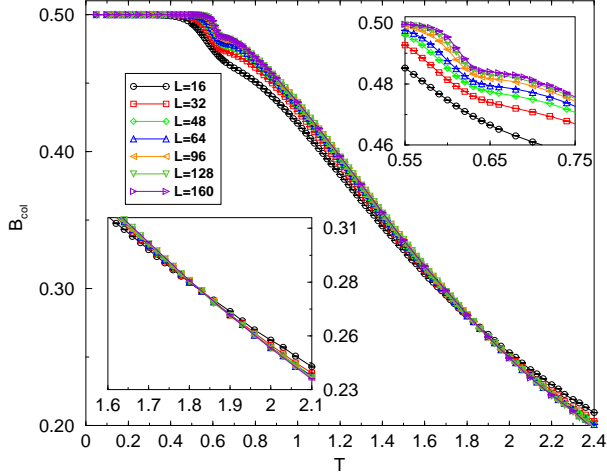


FIG. 17: (Color online) Columnar Binder cumulant  $B_{\text{col}}$  as a function of temperature  $T$  for different system sizes. Right inset: Anomaly near  $T \sim 0.63$ . Left inset: Pseudo-crossing around  $T \sim 1.8$ .

correlations, it appears likely that the second feature at high  $T$  actually disappears in the thermodynamic limit, whereas the first one around  $T \sim 0.63$  subsists. Indeed, whereas both the columnar susceptibility and Binder cumulant are marked at the lowest temperature, the temperature at which  $\chi_{\text{col}}$  peaks is different from the one at which  $B_{\text{col}}$  shows a crossing.

We believe that the plaquette correlations found in Sec. V B 2 affect the finite size behavior of other observables and are in particular responsible for the behaviors observed in the columnar susceptibility and Binder cumulant. The fact that strictly speaking,  $\chi_P$  does not peak where the second peak in  $\chi_{\text{col}}$  is present (even though the

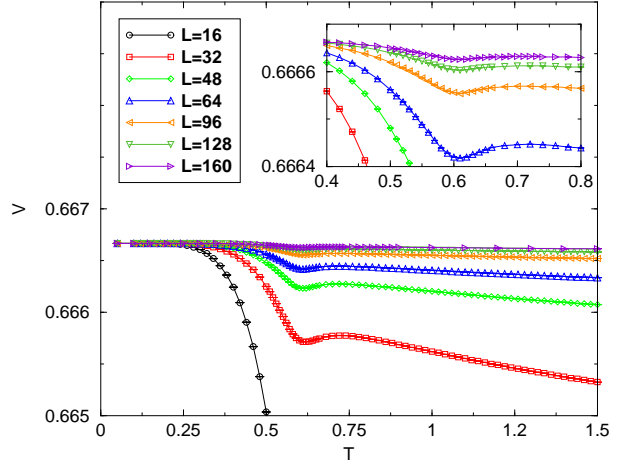


FIG. 18: (Color online) Energy cumulant  $V$  versus temperature  $T$  for different system sizes. Inset: zoom on the large size samples.

latter drifts with system size) might indicate that other types of correlations are also present above  $T_c$ .

In conclusion of this section, we find that the model Eq. (1) shows a unique transition to a columnar order at  $T_c = 0.65(1)$  with no intermediate phase, but with strong plaquettes correlations above  $T_c$ .

## VI. NATURE OF THE PHASE TRANSITION

The model Eq. 1 displaying a phase transition at  $T_c = 0.65(1)$  separating a low  $T$  columnar phase from a high  $T$  phase (that we will describe more carefully in Sec. VII), we now investigate the nature of this phase transition.

### A. Energy cumulant

We first plot in Fig. 18 the behavior versus temperature  $T$  of the energy cumulant [28] :

$$V = 1 - \frac{\langle E^4 \rangle}{3 \langle E^2 \rangle^2}. \quad (43)$$

In both a disordered and in an ordered phase, this cumulant saturates to 2/3 in the thermodynamic limit [28]. This is also the case at the critical point for a second order phase transition (even though the energy distribution is not Gaussian), whereas for a first order transition, it admits a non-trivial minimum (different from 2/3) in the thermodynamic limit [28]. We are not aware of any predictions for a KT transition.

Our results for  $V(T)$  show a clear dip close to the critical temperature  $T_c = 0.65(1)$  for all system sizes, but this minimum scales to 2/3 in the thermodynamic limit as can be clearly seen in the inset of Fig. 18. These results exclude a first order transition.

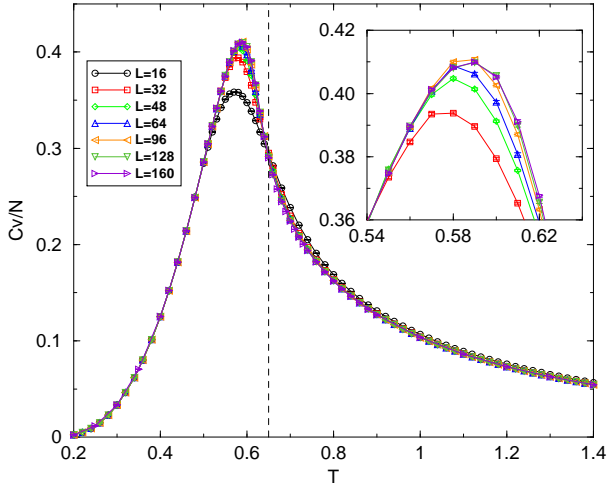


FIG. 19: (Color online) Specific heat per site  $C_v/N$  versus temperature  $T$  for different system sizes. The dashed line indicates  $T_c = 0.65(1)$ . Inset: zoom on the specific heat peak.

### B. Specific Heat

We now consider the second cumulant of the energy, *i.e.* the specific heat per site, defined as :

$$\frac{C_v}{N} = \frac{1}{N} \frac{\langle E^2 \rangle - \langle E \rangle^2}{T^2}. \quad (44)$$

The specific heat per site shows a pronounced peak which does *not* diverge in the thermodynamic limit (see Fig. 19 and its inset). We can see that this peak is located at a temperature  $T \sim 0.59$  different from the critical temperature  $T_c = 0.65(1)$ , denoted by a dashed line in Fig. 19. For a second-order phase transition, we would have expected either a divergence of the specific heat at  $T_c$  (if the critical exponent  $\alpha > 0$ ) or a cusp (for  $\alpha < 0$ ). Our results show that  $C_v$  is completely featureless at  $T_c$ : this is typical of a *Kosterlitz-Thouless transition*. We will see in the following sections that this is naturally expected noticing the nature of the high-temperature phase that we now address.

## VII. HIGH-TEMPERATURE PHASE

It was demonstrated more than 40 years ago that the  $T = \infty$  point of our model (which is the classical dimer covering of the square lattice) is critical: the system possesses correlations functions that decay algebraically with distance [4]. In this section we consider the fate of various correlation functions in the whole high- $T$  region  $[T_c, \infty[$ .

### A. Dimer-Dimer correlation functions

We have calculated two types of dimer-dimer correlation functions in the MC simulations. Both types concern dimers which are chosen for simplicity in the same orientation. We take horizontal dimers without loss of generality. The first correlator which we dub “longitudinal” is the connected correlation function of two horizontal dimers on the same row separated by a distance  $x$  :

$$G^l(x) = \langle \hat{n}_\perp(\mathbf{r}) \hat{n}_\perp(\mathbf{r} + (x, 0)) \rangle - 1/16, \quad (45)$$

where  $\hat{n}_\perp(\mathbf{r}) = 1$  for a horizontal dimer at site  $\mathbf{r}$ , and 0 otherwise. The constant  $1/16$  stands for the dimer density squared. The second one is the “transverse” correlation function of two dimers separated by a distance  $x$  on the same column :

$$G^t(x) = \langle \hat{n}_\perp(\mathbf{r}) \hat{n}_\perp(\mathbf{r} + (0, x)) \rangle - 1/16. \quad (46)$$

At  $T = \infty$ , the exact calculations of Ref. 4 give the asymptotic results

$$G^l(x) \sim (-)^x \frac{1}{\pi^2 x^2} + O(x^{-3}) \quad (47)$$

and

$$G^t(x) \sim \frac{1}{\pi^2 x^2} + O(x^{-3}) \quad x \text{ odd} \quad (48)$$

$$\sim -\frac{1}{\pi^2 x^4} + O(x^{-6}) \quad x \text{ even} \quad (49)$$

For all finite  $T \geq T_c$ , we find that the longitudinal correlation function  $G^l(x)$  remains staggered, and that it decays algebraically, with a decay exponent  $\alpha_d$  that varies continuously with the temperature  $T$ :

$$G^l(x) \sim (-)^x A(T) x^{-\alpha_d(T)} \quad (50)$$

for large  $x$  (with  $A(T)$  an amplitude). In Fig. 20, we represent  $(-)^x G^l(x)$  for four different  $T = 1, 2, 3$  and  $T = \infty$  on a log-log scale to emphasize the power-law decay. The algebraic decays are eventually cut around  $L/2$  due to the PBC (system size is here  $L = 512$ ). The value of the decay exponent  $\alpha_d(T)$  can be estimated from these plots, however the symmetry around  $L/2$  due to the PBC makes a high-precision determination of the exponent difficult, since it would depend on the range of distances used in the fit. We will use alternative methods (TM calculations and winding fluctuations) in Sec. VIII to estimate decay exponents. To show that the different ways of estimating the decay exponents are consistent, we have plotted in Fig. 20 lines corresponding to the decay exponents found in Sec. VIII (at  $T = \infty$ , we take the exact result  $\alpha_d(T = \infty) = 2$ ). These lines are in perfect agreement with the first part of the correlation function  $(-)^x G^l(x)$  which is not affected by the periodicity.

In Fig. 21, we plot the transverse correlation function  $G^t(x)$  for the same  $T$ . We also find here a power-law decay with the same exponent  $\alpha_d(T)$  as for the longitudinal

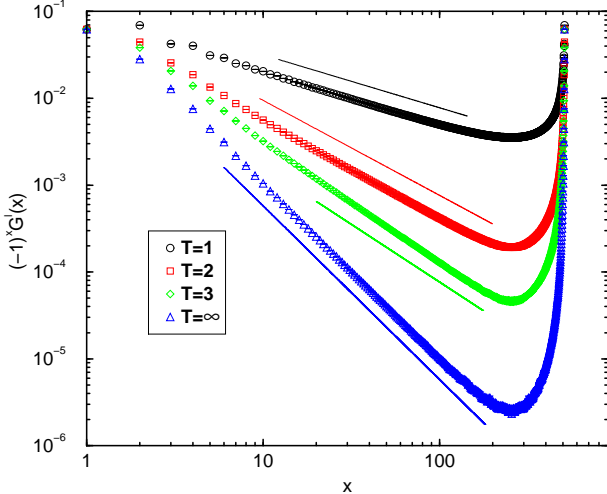


FIG. 20: (Color online) Staggered longitudinal dimer-dimer correlation function  $(-1)^x G^l(x)$  versus distance  $x$  between dimers for four different temperatures  $T$  (log-log scale). The straight lines correspond to decay exponents  $\alpha_d(T)$  calculated in Sec. VIII.

correlation function ( $(-1)^x G^l(x)$  and  $G^t(x)$  essentially coincide for large  $x$ ). Small deviations can however been found at small distances (see  $x < 10$  in Fig. 21), where the data for odd or even  $x$  do not exactly coincide. This odd/even distinction is already present in the  $T = \infty$  case - see Eq. (48) and (49). We find that  $G^t(x)$  is well fitted by the expression:

$$G^t(x) \sim A(T)x^{-\alpha_d(T)} \quad x \text{ odd} \quad (51)$$

$$\sim A(T)x^{-\alpha_d(T)} + B(T)x^{-\omega(T)} \quad x \text{ even} \quad (52)$$

where  $A(T)$  is the same amplitude as the one found for the longitudinal correlation function,  $B(T)$  a negative constant and  $\omega(T)$  a subleading correction exponent for even  $x$ . Our data are compatible with  $\omega(T) \sim 2$ .

## B. Monomer-Monomer correlation function

Besides dimer-dimer correlation functions, it is useful to consider the correlator between *monomers*, which are defined as sites not paired to any neighboring site by a dimer. Monomers are by definition absent in the model, however we can calculate the properties of two test monomers in a background of dimers by considering the monomer-monomer correlation function [4, 19, 29]

$$M(\mathbf{x}) \sim Z(\mathbf{x}), \quad (53)$$

where  $Z(\mathbf{x})$  denotes the number of possible configurations where the two test monomers are separated by a vector  $\mathbf{x}$ . Note that this is exactly the correlation function  $C_{Q_0}(M)$  defined in the TM section IV B (we changed

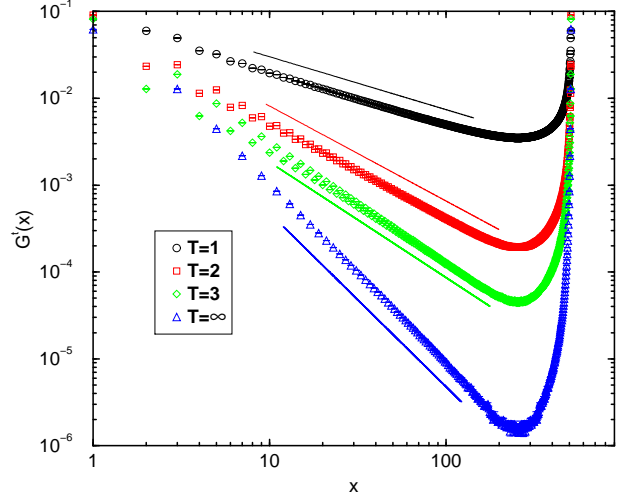


FIG. 21: (Color online) Transverse dimer-dimer correlation function  $G^t(x)$  versus distance  $x$  between dimers for four different temperatures  $T$  (log-log scale). The straight lines correspond to decay exponents  $\alpha_d(T)$  calculated in Sec. VIII. For the  $T = \infty$  curve, the results for even  $x$  have been omitted (as they are negative - see Eq. 49).

notations from  $M$  to  $\mathbf{x}$  and  $C_{Q_0}$  to  $M$  for consistency with previous works). For a bipartite lattice such as the square lattice,  $M(\mathbf{x}) = 0$  if monomers are located on the same sublattice. From now on, we will consider only monomers on opposite sublattices. To simplify calculations, we focus on the case  $\mathbf{x} = (x, 0)$  (two monomers on the same row). The proportionality constant is taken such that  $M(1) = 1$  [4, 19].

At  $T = \infty$ , the exact result  $M(x) \sim x^{-1/2}$  holds in the thermodynamic limit [4]. At finite  $T$ , we can estimate  $M(x)$  with high-precision thanks to the worm algorithm (see Sec. IV A). Results for  $M(x)$  are displayed versus  $x$  on a log-log scale in Fig. 22 for the four temperatures used for the dimer-dimer correlation functions: we also observe here power-laws, with an exponent  $\alpha_m(T)$  that appears to vary continuously with  $T$ :

$$M(x) \sim x^{-\alpha_m(T)}. \quad (54)$$

For the same technical reasons as for the dimer-dimer correlation functions, we do not estimate directly from this plot the values of  $\alpha_m(T)$ , as the error bars would be too large. We will obtain precise estimates of  $\alpha_m(T)$  in the next section VIII, which we already display as straight lines in Fig. 22 to show the good agreement with the real-space measures of  $M(x)$ . As will be understood, we note that whereas  $\alpha_d(T)$  decreases when lowering  $T$ ,  $\alpha_m(T)$  increases (this can be clearly seen with the identical color chart of figures 20, 21 and 22).

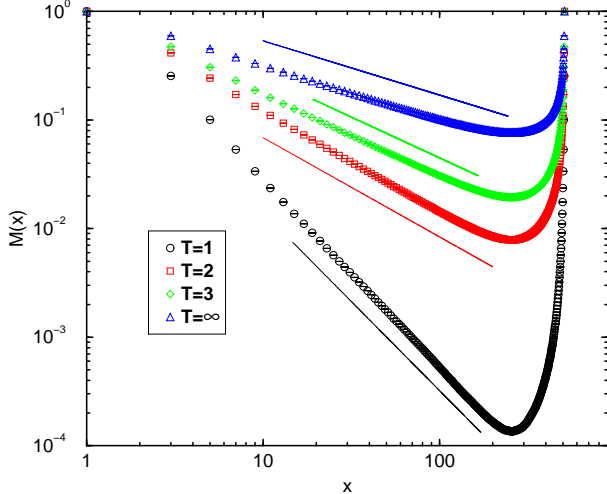


FIG. 22: (Color online) Monomer-monomer correlation function  $M(x)$  versus distance  $x$  between monomers for four different temperatures ( $T$  log-log scale). The straight lines correspond to decay exponents  $\alpha_m(T)$  calculated in Sec. VIII. For the  $T = \infty$  curve, we used the exact result  $\alpha_m(T = \infty) = 1/2$ .

### VIII. THEORETICAL INTERPRETATION

We recapitulate the MC results on the finite- $T$  behavior of the interacting dimer model Eq. (1) with  $v < 0$ : we observe a transition from a high- $T$  critical phase with continuously varying critical exponents to a low- $T$  crystalline phase of dimers. Even though other types of correlations are present (such as plaquette correlations), there is no intermediate phase in-between. The transition is found to be of KT type. The existence of the high- $T$  critical phase, the floating exponents, the KT transition and the dimensionality  $d = 2$  of the problem naturally suggest *Coulomb gas physics* [11]. In the following, we will indeed describe the (non-exact) mapping of the interacting dimer model to a CG that will account for all the above findings. Moreover, thanks to results of CFT and use of TM calculations, we will be able to determine with high-precision the critical exponents  $\alpha_d(T)$  and  $\alpha_m(T)$ , and the associated CG constant.

The following section will also have the advantage of reconciliating different points of view on the model Eq. (1). Readers familiar with height models will find an alternative derivation of the effective height action for dimer configurations. For readers familiar with CG physics, the TM calculations presented here will allow a high precision test of the CG predictions, with a precision probably not reachable in other models. For readers interested in the dimer enumeration problem at  $T = \infty$ , an interesting relationship between dimer winding numbers fluctuations and CG constant will be derived in passing. Finally, for readers coming from the quantum condensed matter community, these results have profound implications for the high- $T$  regime of QDM, as will be discussed

in Sec. IX.

#### A. Mapping to a Coulomb gas

##### 1. Height model

To obtain a CG picture of the interacting dimer model, we first use a *height* description of dimer configurations [6]. Each plaquette of the square lattice is assigned a real-valued height  $z$  in the following way: going counterclockwise around an even (resp. odd) site on the square lattice,  $z$  changes by  $+3/4$  if the bond crossed is occupied by a dimer and by  $-1/4$  if it is empty (resp.  $-3/4$  and  $+1/4$ ). These units are chosen such that a monomer on the even (resp. odd) sublattice corresponds to a dislocation of 1 (resp. -1) in the height. To fix the absolute height, one fixes the plaquette at the origin to have, say,  $z(0) = 0$ . By integrating out the short distance fluctuations of  $z(r)$ , one obtains an effective action  $S_{\text{eff}}[h]$  for the coarse-grained height  $h(r)$ , defined in the continuum, which corresponds to the long-wavelength modes of  $z(r)$ .

*Locality* — The form of this effective action is constrained by the fact that the microscopic model is local in terms of the dimer degrees of freedom. Consider a finite area  $A$  of the system and some fixed coarse-grained height  $h(r)$  for  $r \in A$ . The associated free energy (obtained by summing over all microscopic dimer configurations compatible with the given  $h(r)$ ) should not depend on the dimer positions *outside*  $A$ . However, by shifting the dimers along a closed loop, the dimer configuration inside is unchanged but the microscopic height  $z(r)$  is uniformly shifted by +1 (or -1) for all the plaquettes located inside the loop (and so for the coarse grained height  $h$ ). Doing so for a large loop surrounding  $A$ , one therefore shows that  $S_{\text{eff}}$  must satisfy  $S_{\text{eff}}[h] = S_{\text{eff}}[h+1]$  for any physical  $h$ .

*$\pi/2$  rotation symmetry* — Consider a large but finite square area  $A$  of the lattice with linear even size  $L$ . Outside  $A$ , the dimers are assumed not to cross the boundary of  $A$ . Let  $z(r) = z_0 + d(r)$  be the height inside  $A$  and  $z_0$  the height of the, say, lower left corner of  $A$  [30]. Whatever the dimer locations inside  $A$  (compatible with the constraint above), one can move the dimers *inside*  $A$  by a  $\pi/2$  rotation  $\mathcal{R}$  with respect to its central plaquette.  $z$  is unchanged outside  $A$  but for  $r \in A$  the height is changed to  $z'(r) = z_0 - d(\mathcal{R}(r))$ . Now we take a smooth height profile  $h(r \in A)$  and evaluate the associated free energy  $S_{\text{eff}}[h]$  by summing over all microscopic dimerizations giving the same coarse grained height  $h$ . By the rotation described above, we know that another height  $h'(r) = -h(\mathcal{R}(r))$  corresponds to the same set of dimerizations of  $A$ , up to a rotation. Because  $\mathcal{R}$  is a symmetry of the lattice and of the dimer-dimer interactions, both  $h$  and  $h'$  must have the same free energy and we get  $S_{\text{eff}}[h] = S_{\text{eff}}[-h]$ . Here we ignored boundary effects at the edge of  $A$ , which should be negligible for a large

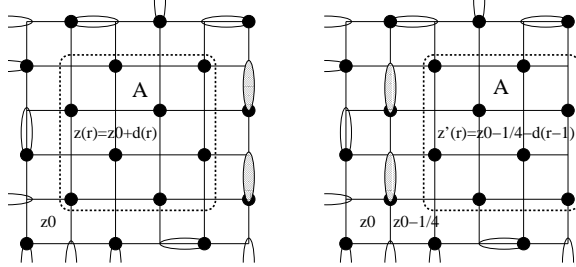


FIG. 23: Assuming that the column of sites located immediately to the right side of the area  $A$  is occupied by vertical dimers (shaded) and that no dimer crosses the boundary of  $A$  (dashed line), one can shift the whole area by one lattice spacing to the right. The vertical dimers are then moved to the left side. Such a “local” translation changes the height profile inside  $A$  from  $z(r) = z_0 + d(r)$  to  $z'(r) = z_0 - \frac{1}{4} - d(r-1)$ . The change  $d(r) \rightarrow -d(r)$  reflects the fact that the two sublattices are exchanged inside  $A$ .  $z_0$  is the height at the lower left corner of  $A$  before the translation.

enough area.

*Translation symmetry*—In addition to the assumption that no dimer crosses the boundary of  $A$ , we assume that some dimers occupy all the vertical bonds on the right side of  $A$  (shaded dimers in the left panel of Fig. 23). One can shift the dimers of  $A$  by one lattice spacing to the right provided that the column of dimers on the right side of  $A$  is put back on the left side after the translation (shaded dimers in the right panel of Fig. 23). If the height inside  $A$  is  $z(r) = z_0 + d(r)$ , the new height after the translation is  $z'(r) = z_0 - \frac{1}{4} - d(r-1)$ . As before,  $z_0$  is the height of the lower left corner of  $A$  before the move (and  $z_0 - \frac{1}{4}$  after the translation). Again, we evaluate the free energy  $S_{\text{eff}}[h]$  associated to a smooth height profile by summing over all microscopic dimerizations giving the coarse-grained height  $h$ . From the “local translation” above, one shows that the smooth height  $h'(r) = -\frac{1}{4} - h(r-1) \simeq -\frac{1}{4} - h(r)$  corresponds to the same set of dimerizations of  $A$ , but shifted by one lattice spacing. Because of the *translation invariance* of the model, both coarse-grained height profiles therefore have the same free energy:  $S_{\text{eff}}[h] = S_{\text{eff}}[-h - \frac{1}{4}]$ . As before we ignored boundary effects at the edge of  $A$ . We also neglected the variations of  $h$  at the lattice spacing scale:  $h(r) \simeq h(r+1)$ . This is natural for a smooth height, obtained from a microscopic (and discrete)  $z(r)$  by filtering out short wavelength modes.

From the discussion above, it appears that lattice symmetries of the dimer model implies not only spatial symmetries for the effective height model but also some *periodicity* of the free energy in the height space. A similar result was previously obtained by Henley and coworkers using the concept of “ideal states” [31].

Combining the constraints of translation and rotation symmetries, we get that  $h \rightarrow -h$  and  $h \rightarrow h + \frac{1}{4}$  should

keep the effective action invariant. This shows that the only allowed “potential” terms are  $\cos(2\pi ph)$  with  $p$  an integer multiple of 4. As only long-wavelength modes ( $k \ll 1$ ) are kept in a coarse-grained height, only terms with a minimal number of space derivatives are important. This naturally leads to an “elastic” term  $(\nabla h)^2$ . We eventually get a sine-Gordon model for the coarse-grained height:

$$S_{\text{eff}} = \int d\mathbf{r} \left[ \pi g |\nabla h(\mathbf{r})|^2 + \sum_{p=4,8,12,\dots} V_p \cos(2\pi ph(\mathbf{r})) \right] \quad (55)$$

So far we only invoked symmetry arguments to constrain the form of the effective action. It turns out that the elastic and potential terms with  $p = 4$  have a simple physical interpretation in terms of the dimer model. The gradient term favors “flat” heights. There are indeed more dimer configurations corresponding to a flat average height than a tilted one. This comes from the fact that a dimer shift along a closed loop is possible only if the height is constant (up to small discretization effect) along the loop. Thus, there is more room for dimer moves if the average slope is small (in which case there are many small “iso- $h$ ” loops available) than if the slope is large (fewer “iso- $h$ ” curves). As for the  $\cos(8\pi h)$  terms, it has 4 minima ( $h = \frac{1}{8}, \frac{3}{8}, \frac{5}{8}, \frac{7}{8}$ ) which precisely coincide with the average height of the 4 columnar configurations (ground-states) which minimize the dimer-dimer interaction energy (see Fig 3). The model therefore describes a combination of entropy and energy (locking) effects.

It is a standard result [32] that in 2D the relevance in the Renormalization Group (RG) sense of the cosine term depends on the period and on the stiffness constant  $g$  [33]. The cosine term is relevant (and locks the height) if  $g > p^2/4$  whereas it renormalizes to zero when  $g < p^2/4$ . In the latter case the long-distance theory is a free field (elastic term only) and the system is critical (“rough” in the height model terminology). The transition between the two phases is of the KT type. For completeness, this classic RG calculation is reproduced in Appendix A.

## 2. Coulomb gas

It is well-known that the sine-Gordon model is equivalent to a (low-density) one-component CG [11]. This standard mapping is reproduced in Appendix B. This point of view has the advantage (over the sine-Gordon model described above) that it provides a framework to understand the role of the (here suppressed) monomers in the model, as well as other operators or correlations.

In the mapping from the sine-Gordon model to a CG model, the height field is conjugate to the *electric* charge density. Similarly, it can be shown that magnetic charges correspond to topological defects (dislocations) in the height. A dual magnetic charge  $m = 1$  (resp.  $m = -1$ ) corresponds to a dislocation in the height field, which can

be inserted “by hand” through the inclusion of monomers on the even (resp. odd) sublattice or through appropriate boundary conditions (see the discussion in Sec. IV B). The exponent [34] associated to the insertion of a particle with electromagnetic charge  $(e, m)$  is given by [11]

$$\alpha(e, m) = e^2/g + gm^2, \quad (56)$$

where  $g$  is the *Coulomb gas coupling constant*. The normalization of  $g$  and of the height field in Eq. (55) have been chosen such that  $e$  and  $m$  are integers and that standard expressions [11] for  $g$  are recovered.

In the CG picture, inserting an electric charge  $e$  is implemented by a vertex operator  $V_e(\mathbf{r}) =: \exp(2i\pi e h(\mathbf{r}))$ : appearing in the Fourier expansion of any operator periodic in the coarse-grained field. Such a term with  $e = 1$  actually appears as a continuum limit contribution in the definition of the dimer operator [35]: this allows to identify the continuum limit of the dimer number as an operator with electric charge  $e = 1$ . To magnetic charges (monomers) correspond dual operators  $\hat{h}(\mathbf{r})$ ; however the fugacity for these magnetic charges is fixed to zero as we consider close-packed dimers. The dimer-dimer correlation function decays with an exponent related to the dimension of the  $e = 1$  operator,  $\alpha_d = \alpha(1, 0) = 1/g$ , and the monomer-monomer correlation function decays with the exponent  $\alpha_m = \alpha(0, 1) = g$ . This leads in particular to the prediction  $\alpha_d = 1/\alpha_m$ , independently of  $T$  [12].

The effective coupling constant  $g(T)$  varies with  $T$  to account for the continuously varying exponents. It can be calculated via the above mentioned relations with decay exponents or via fluctuations of winding numbers (see Sec. VIII C). As usual in a CG description, it is useful to have an external exact result to fix the coupling constant: here the calculations of Refs. 2, 4 give  $g(T = \infty) = 1/2$ .

Another insight of the CG picture is about the relevance of the locking potential  $V_p$  in Eq. (55): the identification with the vertex operator of an electric charge  $p$  immediately indicates [11] that it will become relevant for  $g \geq g_c(p) = \frac{p^2}{4}$  (this is the same result as obtained within the RG of Appendix A). In our model,  $p = 4$  and  $g$  thus increases from  $1/2$  at  $T = \infty$  to  $g(T_c) = g_c(p = 4) = 4$  at the critical point. This also means that locking potential terms with higher values of  $p$  will always be less relevant and can be ignored in the present model.

We finally note that an equivalent route leading to the same CG model is to consider the low- $T$  phase. The system has a four-fold ground-state degeneracy. At low  $T$ , a finite system is mainly composed of large domains where all the dimers are aligned in one of the four possible columnar states of Fig. 3. One can associate to each domain orientation a  $q = 4$  “clock spin”. One could therefore naively expect a transition in the 2D  $q = 4$  state clock model universality class. The  $q$ -state clock model is well known to map to a Coulomb gas with (unconstrained) integer magnetic charges and electric charges multiples of  $q$  [11]. The key point here is that due to the absence of monomers in our model, there cannot be isolated points (sites) around which this clock-spin can

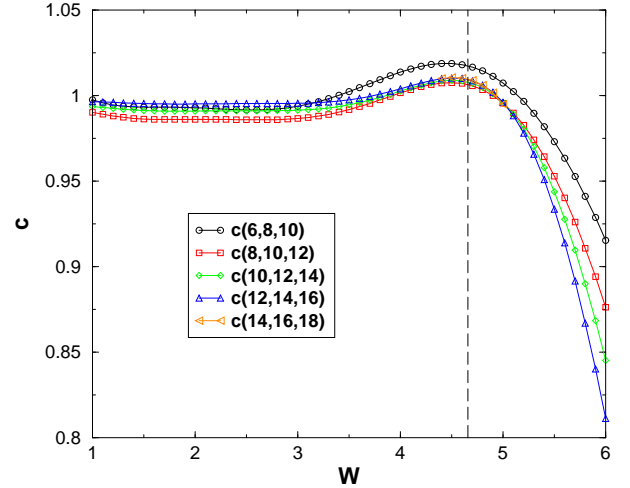


FIG. 24: (Color online) Three-point fits  $c(L - 4, L - 2, L)$  for the central charge, as a function of  $W$ . The dashed line indicates  $T_c$  as found by the Monte Carlo simulations.

make a  $2\pi$  rotation passing by the four possible ground states. This is nicely illustrated in another context in Ref. 36. In other words, we are considering a  $q = 4$  state clock model *with no topological defects*. Magnetic charges are therefore absent in the associated CG and we arrive at the same CG picture described above: electric charges can only be multiples of 4 and magnetic charges are absent.

## B. Transfer Matrix calculations

TM calculations are perfectly suited to validate this CG scenario, thanks to the conformal invariance results Eq. (34) and (35).

### 1. Fundamental exponents

In Fig. 24, we show the finite-size estimates of the central charge  $c$  as a function of  $W \equiv e^{-v/T}$ . The results shown are three-point fits based on Eq. (35) with a  $1/L^4$  correction added. Indeed, such a non-universal correction is predicted by conformal invariance, and is known to greatly improve the rate of convergence. The data show a clear  $c = 1$  plateau for  $1 \leq W \leq W_c$ , where we estimate  $W_c = 4.5(1)$  from the intersections of the curves. For  $W > W_c$  the curves level off to zero, with the drop getting sharper with increasing strip width  $L$ : this signals the transition to non-critical behavior. The estimate of  $W_c$  is in perfect agreement with the MC estimate of  $T_c$ .

In Fig. 25 we show the finite-size estimates of the monomer exponent  $X_1 = \alpha_m/2$  as a function of  $W$ . The results shown are two-point fits based on Eq. (34) for

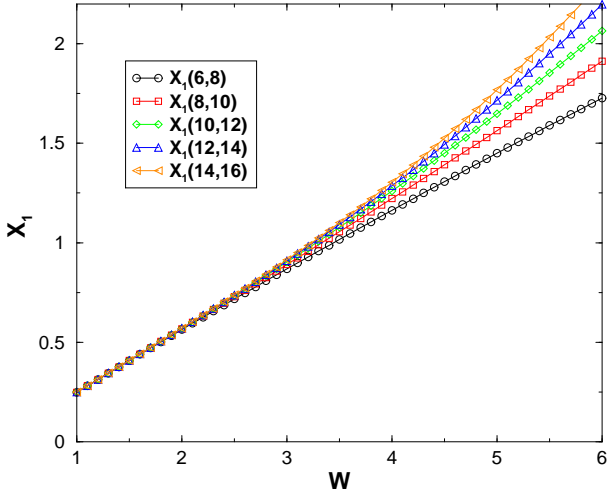


FIG. 25: (Color online) Two-point fits  $X_1(L - 2, L)$  for the monomer exponent, as a function of  $W$ .

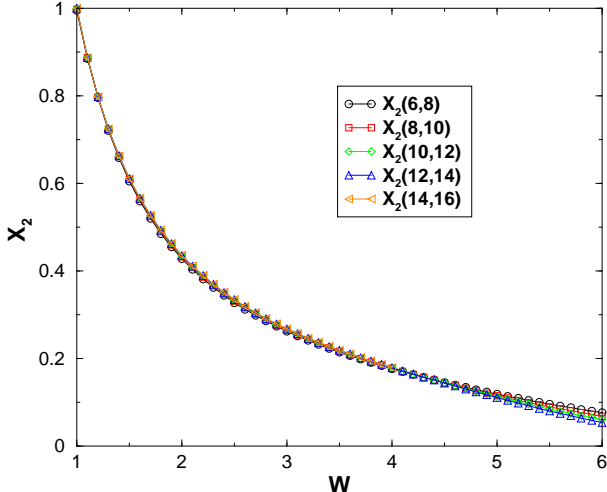


FIG. 26: (Color online) Two-point fits  $X_2(L - 2, L)$  for the dimer exponent, as a function of  $W$ .

$Q_0 = 1$  with, once again, a  $1/L^4$  correction added. The agreement with the result  $X_1 = 1/4$  (see Section III F) for  $W = 1$  is very clear. Within the critical region  $W \in [1, W_c]$ , the data can readily be extrapolated to the thermodynamic limit  $L \rightarrow \infty$ , and one finds that  $X_1$  is a monotonically increasing function of  $W$  that eventually takes the value  $X_1(W_c) = 2$ . So the monomer perturbation is marginal at  $W_c$  and relevant in the critical region, as predicted by the CG. For  $W > W_c$  the extrapolation in  $L$  of the numerical data does not work well, as could be expected from the non-critical behavior predicted in this region.

Fig. 26 shows the finite-size estimates of the dimer exponent  $X_2 = \alpha_d/2$  as a function of  $W$ , based on the first

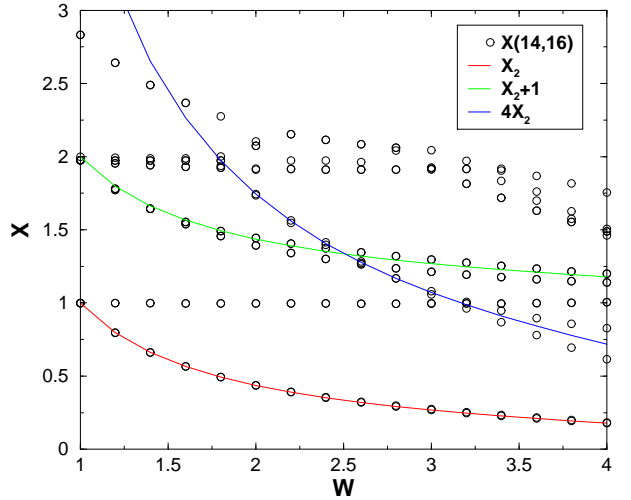


FIG. 27: (Color online) Two-point fits  $X(14, 16)$  for the first 15 exponents in the  $Q = 0$  block, as functions of  $W$ . All observed exponents are simply related to the fundamental dimer exponent  $X_2$ .

two eigenvalues in the  $Q = 0$  block. There is an excellent agreement with the result  $X_2 = 1$  (see Section III F) for  $W = 1$ . Inside the critical region  $W \in [1, W_c]$ , the data decrease monotonically, and one has to a very good precision  $X_1 X_2 = 1/4$  independently of  $W$ , confirming the CG scenario involving only a single coupling constant  $g$ . An estimate for the location of the critical point  $W_c$  can be obtained from the crossings of the curves, and is consistent with the one given above.

## 2. Higher dimer exponents

To analyze the agreement with the CG scenario in more detail, we show in Fig. 27 the exponents  $X$  obtained from the first 15 gaps in the  $Q = 0$  block. The first of these coincides with the fundamental dimer exponent  $X_2$  discussed above. This level exhibits a two-fold degeneracy which is almost exact at finite size. The identity operator is observed to have descendants at level 1 and 2 (*i.e.* operators with constant  $X = 1$  and  $X = 2$ ), in agreement with CFT.

More interestingly, all other exponents appear to be of the form  $p^2 X_2 + q$ , for integers  $p \geq 2$  and  $q \geq 0$ . In the CG scenario, this is accounted for by operators of electric charge  $p$  times that of the fundamental one, and their descendants. Inevitably, these higher operators are slightly less well determined in finite size, and the splittings of the degeneracies which would be exact in the thermodynamic limit are somewhat larger. In the figure, we have shown in solid line style the finite-size data for  $X_2$  (corresponding to  $p = 1$ ),  $X_2 + 1$  (its first descendant) and  $4X_2$  (the  $p = 2$  electric exponent). The agreement with the numerical data is very fine.

To summarize, the data of Fig. 27 provide strong evidence that the CG description of the model is correct and complete.

### 3. Including monomers

The generalization of the dimer model to finite monomer fugacity was first studied by TM calculations in the grand canonical ensemble in Ref. 12. We give here a more detailed analysis. We also mention a very recent work by Papanikolaou, Luijten and Fradkin [17] who independently consider the finite doping transition in this model.

The monomer exponent  $X_1$  is RG relevant (*i.e.*  $X_1 < 2$ ) for  $1 \leq W < W_c$ . This means that the critical phase of the close-packed dimer model is unstable toward doping with monomers. We have verified numerically that there is no critical behavior for  $W \in [1, W_c)$  and finite monomer fugacity  $\xi$ . This means that the RG flow will be toward the trivial non-critical fixed point at  $\xi = \infty$ .

However,  $X_1$  is marginal ( $X_1 = 2$ ) exactly at  $W = W_c$ , and thus one may suspect, as announced in Ref. 12, that allowing for a finite monomer density will produce another critical line emerging from  $W_c$ . To test this suspicion, we have adapted the TM to accommodate for monomers with Boltzmann weight  $\xi$ . The weight of a pair of aligned dimers is still  $W = e^{-v/T}$  with  $v = -1$ .

Despite of this modification the basis states can still be described in terms of the edge occupation numbers introduced in Sec. III G. The main difference is in the dimer constraint: if a vertex is occupied by a monomer, none of its four incident edges may be occupied by a dimer. It should be noted that allowing for monomers will couple the different blocks  $T_Q$  of the TM. Accordingly, the dimension  $\dim(T)$  of the modified TM is larger than in the pure dimer case for which one could diagonalize sector by sector. We have therefore restricted the study of the monomer-doped model to widths  $L \leq 16$ . The analytic expression for  $\dim(T)$  has been given in Eq. (37) above.

In Fig. 28 we show rough scans of the effective central charge  $c_{\text{eff}}$  as a function of  $T$ , for various values of  $\xi$  and rather small sizes  $L$ . We observe that for each value of  $\xi$ , there exists a temperature  $T(\xi)$  for which  $c_{\text{eff}}$  goes through a maximum. The finite-size corrections to  $T(\xi)$  are found to be very small. We interpret the curve  $T(\xi)$  as a line of fixed points which correspond to the phase transition between high and low monomer density.

As the maximum in  $c_{\text{eff}}$  becomes sharper with increasing system size (not shown), the fixed points  $T(\xi)$  are RG unstable to small variations in the parameters  $(\xi, T)$ . This means that points on the low- $\xi$  side of the transition will renormalize toward vanishing monomer density, but this phase will be non-critical (crystalline phase) since the temperature is lower than the critical temperature in the pure dimer model. Points on the high- $\xi$  side of the transition will renormalize toward infinite  $\xi$  as before. Note that when  $\xi$  increases,  $T(\xi)$  decreases. This was to

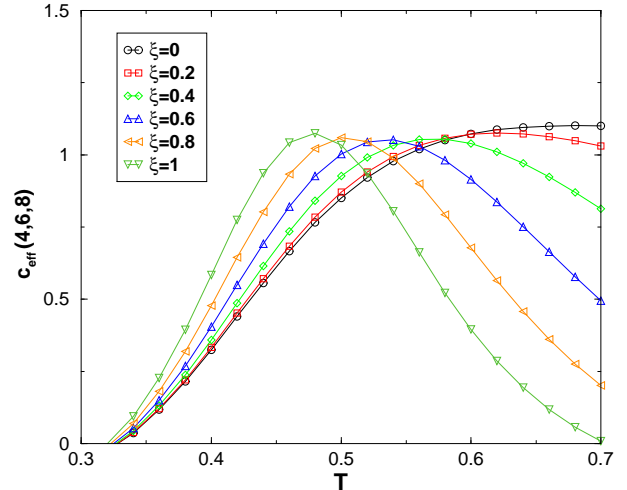


FIG. 28: (Color online) Temperature scans of the effective central charge  $c_{\text{eff}}(4, 6, 8)$  for various values of the monomer weight  $\xi$ .

$\xi$	0.0	0.2	0.4	0.6	0.8	1.0
$T(\xi)$	0.6635	0.6125	0.5710	0.5360	0.5055	0.4795
$\xi$	1.4	1.8	2.6	4.0	8.0	
$T(\xi)$	0.4355	0.4015	0.3515	0.2970	0.2265	

TABLE II: Phase transition temperature  $T(\xi)$  in the model where monomers are allowed with a weight  $\xi$ . The error bar on the values of  $T(\xi)$  is of the order  $\pm 0.0002$ .

be expected, since when the dimers are diluted by more and more monomers, it becomes harder for them to align at a given temperature.

We have determined  $T(\xi)$  by taking these temperature scans of Fig. 29 to larger sizes (up to  $L = 16$ ) and carefully studying the finite-size effects. Our final results for the phase transition temperatures are given in Table II.

To determine whether the phase transition curve  $T(\xi)$  corresponds to a critical behavior, we show in Fig. 29 the effective central charge as a function of  $T(\xi)$  for several different system sizes. We observe that there exists a temperature  $T_*$  such that  $c \simeq 1$  for  $T(\xi) > T_*$ . Determining  $T_*$  from this figure is a little delicate, since even for the lowest value of  $T$  shown, the finite-size effects are such that  $c_{\text{eff}}$  decreases with increasing  $L$ . We can however give a first rough estimate:

$$T_* = 0.35 \pm 0.05. \quad (57)$$

We interpret the role of  $T_*$  as follows: For  $T > T_*$ , the curve  $T(\xi)$  describes a line of second-order (continuous) phase transitions with  $c = 1$ , whereas for  $T < T_*$ , the phase transition becomes first-order (discontinuous). This means that  $(\xi_*, T_*)$  is a *tricritical* point. The tricritical nature of this point is further corroborated by an easy domain-wall argument showing that the transition at  $T = 0$  is necessarily discontinuous [12].

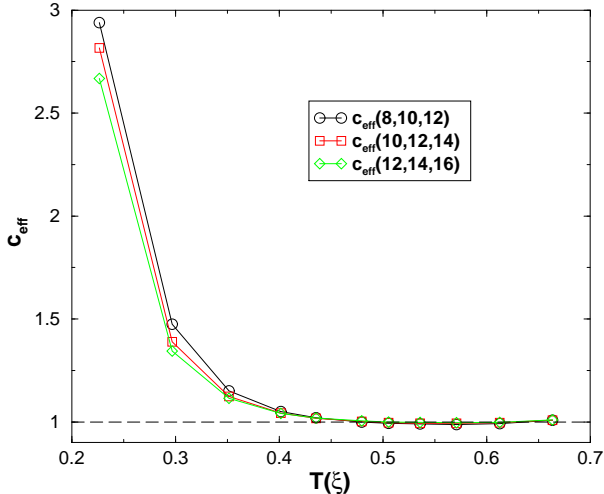


FIG. 29: (Color online) The effective central charge as a function of  $T(\xi)$ . The dashed line denotes  $c_{\text{eff}} = 1$ .

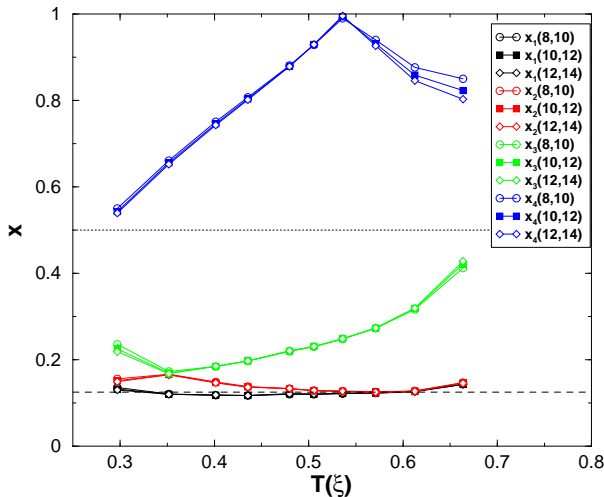


FIG. 30: (Color online) The lowest four scaling dimensions  $x(L-2, L)$  along the critical curve  $T(\xi)$ . The dashed and dotted lines denote the values  $x = 1/8$  and  $x = 1/2$  respectively.

To determine the universality class of the critical part of the curve  $T(\xi)$ , we show in Fig. 30 estimates for the lowest four scaling dimensions (denoted  $x_1 \leq x_2 \leq x_3 \leq x_4$ ) as functions of  $T(\xi)$ . A conspicuous feature is that  $x_1 \simeq 1/8$  is almost independent of  $T(\xi)$ , and that  $x_2$  is almost degenerate with  $x_1$ . The existence of a constant exponent  $x = 1/8$  (first noted in Ref. 12) and other interaction-dependent exponents, is characteristic of the two-dimensional Ashkin-Teller [37] (AT) model. We therefore conjecture that the critical curve  $T(\xi)$  is *in the universality class of the AT model*.

To test this conjecture and make it more precise, we

recall some facts about the isotropic, selfdual AT model, following section 12.9 of Baxter's book [38]. The AT model is originally defined in terms of two Ising models, each with coupling constant  $K$ , that interact via a four-spin (energy-energy) coupling  $K_4$ . Defining  $\omega_1 = \exp(-K_4)$  and  $\omega_3 = \exp(K_4 - 2K)$ , one finds, after a long series of transformations, that the model is equivalent to a six-vertex model with parameters  $a = b = \sqrt{2}\omega_1$  and  $c = \sqrt{2}(\omega_1 + \omega_3)$ . The anisotropy parameter  $\Delta$  of the corresponding XXZ spin chain reads

$$\Delta = 1 - \frac{1}{2} \left( 1 + \frac{\omega_3}{\omega_1} \right)^2 = 1 - 2 \cos^2 \left( \frac{\pi y}{4} \right), \quad (58)$$

where the second equality parametrizes only the critical regime  $|\Delta| \leq 1$ , through the parameter  $y \in [0, 2]$ . We note that  $y = 0$  corresponds to a KT transition. The original couplings,  $K$  and  $K_4$ , are only real and finite for  $y \in [0, 4/3]$ , but from the point of view of the six-vertex model nothing special happens at  $y = 4/3$ . The critical exponents of the AT model differ subtly from those of the equivalent six-vertex model. There are two magnetic-type exponents, which in our notation read  $x_H^{(1)} = 1/8$  and  $x_H^{(2)} = \frac{1}{8-4y}$ , and a temperature-like exponent  $x_t = \frac{1}{2-y}$ .

We now claim that the critical line  $T(\xi)$  corresponds to the AT model with  $y \in [0, 3/2]$ . Moreover, we identify  $x_1 = x_2$  of Fig. 30 with  $x_H^{(1)}$  in the AT model,  $x_3$  with  $x_H^{(2)}$ , and  $x_4$  with  $x_t$  (the latter identification is only on the low- $T$  side of the level crossing visible in the figure; for higher  $T$  we identify  $x_t$  with the analytic continuation of  $x_4$ ). The parameter  $y$  is an (unknown) increasing function of  $T$ , taking the values  $y = 0$  at  $T = T_*$  and  $y = 3/2$  at  $T = T_c$ .

Using Fig. 30, we can now identify  $T_*$  either from  $x_3 = 1/8$  or from  $x_4 = 1/2$ . These two determinations are consistent, but the latter leads to the best final estimate of the tricritical point:

$$T_* = 0.29 \pm 0.02, \quad (59)$$

more precise than the first estimates of Eq. 57 and of Ref. 12. For  $y = 0$ , the original couplings of the AT model satisfy  $K = K_4$ , meaning that the two constituent Ising models couple strongly so as to give a single four-state Potts model. We conclude that the transition at  $T_*$  is in the universality class of the critical ferromagnetic four-state Potts model. Note that this identification is consistent both with the tricritical nature of the transition, and with the existence of a RG marginal direction in the Potts model [39].

Meanwhile, for  $y = 3/2$  we have  $x_H^{(1)} = 1/8$  and  $x_H^{(2)} = 1/2$ . This is in nice agreement with the values of the first two electric-type exponents as obtained from the Coulomb gas of the pure dimer model at  $T = T_c$ . Moreover,  $x_t = 2$  becomes marginal and can be identified with the monomer operator, which is responsible for the transition.

As a last check of the AT identification, consider the point  $y = 1$ , where  $K_4 = 0$  and  $K = \frac{1}{2} \ln(1 + \sqrt{2})$ , so that the model decouples into two non-interacting critical Ising models. Here one has  $x_H^{(2)} = 2x_H^{(1)} = 1/4$  and  $x_t = 1$ . One can verify from Fig. 30 that this indeed happens at the same temperature,  $T_{\text{Ising}} \simeq 0.54$ .

The analysis presented in this section is in agreement with the results of Ref. [17].

### C. Winding number fluctuations and Coulomb gas constant

In this section, we derive an analytical relationship between the coupling constant  $g$  of the CG in the high- $T$  region and the fluctuations of dimer winding numbers (to be defined below). As winding number fluctuations are easily accessible in MC simulations, this allows for an independent calculation of the CG coupling constant that can be compared with TM calculations.

Orienting the dimers from the odd sublattice toward the even sublattice defines a fictitious “magnetic field”  $\vec{B}$  on each bond [7]. Because each site has exactly one dimer, the lattice divergence of this magnetic field is  $\text{div} \vec{B} = 1$  (resp. -1) on the even (resp. odd) sublattice. As a consequence (Gauss law), the flux of  $\vec{B}$  through a contractible loop (with as many sites from each sublattice) is zero in any dimer covering [40]. However, the fluxes  $W_x$  and  $W_y$  through the two (non-contractible) cycles winding around the torus are two non-trivial integers. In the following, we denote  $P(W_x, W_y)$  the probability to observe a dimer configuration with winding numbers  $W_x, W_y$ .

In the continuum limit, this probability can be obtained in the high- $T$  regime where the dimer configurations are coarse-grained into a free field [41]. In the height representation of Sec. VIII A 1, the field  $h$  is defined by the integral of its derivative. The winding number across a cycle is given by this integral along the cycle. The probability  $P(W_x, W_y)$  is the ratio of the partition function restricted to fields having winding numbers equal to  $W_x, W_y$  across the two cycles of the torus:  $Z_{W_x, W_y}$ , divided by the total partition function  $\sum_{W_x, W_y \in \mathbb{Z}} Z_{W_x, W_y}$ .

This ratio can be evaluated as follows: one separates the height field into a classical and a fluctuating part  $h = h_{\text{cl}} + \delta$  where  $h_{\text{cl}}$  is the solution of the equations of motion (a harmonic function) carrying the two winding numbers  $W_x, W_y$ , and  $\delta$  is a fluctuating field with no discontinuity.  $h_{\text{cl}}$  being a solution of the equations of motion, the crossed term disappears from the action and the free part of the action Eq. (55) is the sum of a classical part and a fluctuating part which does not depend on the winding numbers. As a result, the partition function  $Z_{W_x, W_y}$  factorizes into a classical part  $Z_{W_x, W_y}^{\text{cl}}$  and a fluctuating part  $Z'$ , which being independent of the winding number, factorizes out of the probability  $P(W_x, W_y)$ .

On a square torus of size  $L_x, L_y$ , the classical height

configurations are given by:

$$h(x, y) = x \frac{W_x}{L_x} + y \frac{W_y}{L_y}, \quad (60)$$

and the probability is obtained by substituting this field in the expression of the Boltzmann weight:

$$P(W_x, W_y) = \frac{e^{-\pi g((\frac{W_x}{L_x})^2 + (\frac{W_y}{L_y})^2)L_x L_y}}{\sum_{n, m \in \mathbb{Z}} e^{-\pi g((\frac{n}{L_x})^2 + (\frac{m}{L_y})^2)L_x L_y}}. \quad (61)$$

The quadratic fluctuation of the winding number across the direction  $x$  is thus given by:

$$\langle W_x^2 \rangle = \frac{\sum_{n \in \mathbb{Z}} n^2 e^{-\pi g n^2 (L_y/L_x)}}{\sum_{n \in \mathbb{Z}} e^{-\pi g n^2 (L_y/L_x)}}. \quad (62)$$

In the high- $T$  phase of the dimer model, *short-distance* properties are of course *not* described by a free height field. However, a local dimer move cannot change the winding number and we expect that the precise (non-Gaussian) nature of the local fluctuations will not affect winding number observables.  $\langle W_x^2 \rangle$  is related to (fluctuations of) the global slope of the height profile. It can be expressed using the Fourier modes  $|k| \ll 1$  of the height field only [31] and these are precisely those described by the Gaussian action.

In the non interacting case ( $T = \infty$ ) where  $g = 1/2$ , Eq. (62) has recently been derived using the Pfaffian expression of the partition function by C. Boutillier and B. de Tilière [42]. For other values of  $T$ , it allows to calculate through MC simulations the temperature dependence of the coupling constant  $g$ , which can be compared with the one obtained from dimer and monomer exponents calculated via the TM (see Sec. VIII B 1). The temperature dependence of  $g(T)$  obtained by the three methods match perfectly as can be seen in Fig. 31, where the three curves basically overlap. The value of  $g$  at  $T_c$  (denoted by a dashed line in the figure) is  $g_c = g(T_c) = 4.0(2)$ , in agreement with the CG prediction  $g_c = 4$ . The CG analysis and the free field calculation Eq. (62) are therefore entirely validated.

## IX. DISCUSSION

### A. Connection to other classical models

With the interpretation of Sec. VIII A 2, the interacting classical dimer model is naturally related to other scalar-field models displaying a CG behavior [11]. Even if it is not probably exactly solvable, its definition puts it among the most simple ones, along with the XY or 6-vertex models. Moreover, it can be quite naturally extended (*e.g.* by changing the sign of interactions, going to other geometries), which allows to test various features of the CG.

The model Eq. (1) also admits a height description (Sec. VIII A 1), which relates it to a variety of spin

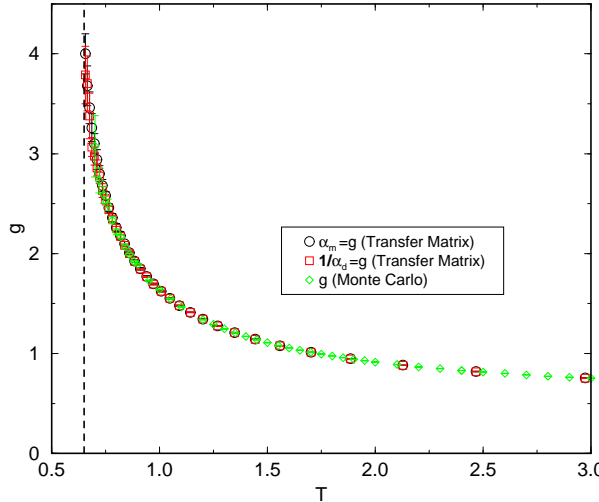


FIG. 31: (Color online) Coulomb gas coupling constant  $g$  as a function of temperature  $T$  obtained via TM (through exponents  $X_1$  and  $X_2$  - see Sec. VIII B 1) and MC calculations (thanks to Eq. 62).

and Solid-On-Solid models (see Ref. 31 and references therein) which display the same physical behavior. We believe this interacting dimer model offers several advantages over these models: (i) its definition is quite simple and natural, (ii) it admits two exact points (at zero and infinite temperature), (iii) *very efficient* numerical simulations are possible (thanks to the directed-loop algorithm [19] for the MC simulations and to the relative small size of the configuration space for the TM calculations).

Concerning numerical simulations of height-like models, we find that the height description is not strictly necessary to obtain reliable numerical results (as opposed to Ref. 31c). Henley and coworkers [31] find the height representation particularly useful because it allows for example to calculate the stiffness (or CG) constant  $g$  via the long-wave lengths fluctuations of the Fourier transform of the height field. We have proposed here an alternative method to obtain  $g$  via the fluctuations of the winding number (see Sec. VIII C), which has the advantage of not involving any fitting procedure.

Concerning the physics of classical dimers, the analysis presented here can probably be extended to the recent results of Sandvik and Moessner [19] on non-interacting models with longer-range dimers. For models with dimers allowed between next-nearest neighboring sites, the bipartite nature of the lattice is lost and the (dislocation-free) height mapping no longer valid: correlations become exponential. For models with a fraction of dimers allowed between fourth-nearest-neighbors, both bipartiteness and height descriptions are present: the system stays critical. There, Ref. 19 finds that the monomer-monomer decay exponent continuously varies (from  $\alpha_m = 1/2$  to  $\alpha_m = 1/9$ ) with the fraction (fu-

gacity  $w_4$ ) of longer-range dimers: this is naturally explained in our framework by considering the variation of the CG constant  $g$  with  $w_4$  - which in turns controls the monomer-monomer decay exponent. It is also found that the dimer-dimer correlation keeps its  $1/r^2$  behavior. This last finding was accounted for in Ref. 19 by considering the “dipolar” terms in the dimer-dimer correlation functions. The corresponding part of the dimer-dimer correlation function continues to vary as  $r^{-2}$  whereas the vertex contribution [35] scales as  $r^{-1/g(w_4)}$ . The long-distance behavior observed in the numerics is therefore dominated by the largest exponent between both; here it is 2. This is reminiscent of spin-spin correlation functions of the XXZ quantum spin chain [43] where the uniform part of the  $\langle S^z(0)S^z(r) \rangle$  correlation function decays as  $1/r^2$  whereas the staggered part decays as  $1/r^{f(\Delta)}$  where  $f$  is a continuous function of the anisotropy parameter  $\Delta$ .

Finally, we remind that the interacting dimer model Eq. (1) was introduced in the context of liquid crystal physics. By means of a low- $T$  expansion, Poland and Swaminathan estimated in Ref. 13b the transition temperature to be  $T_c = 0.61(1)$ , quite close to the actual result. However, they incorrectly stated at that time that the transition was Ising-like (second order) and did not realize the critical nature of the high- $T$  phase.

## B. Implications for finite temperature properties of the Quantum Dimer Model on the square lattice

The classical model naturally offers informations about the finite- $T$  properties of QDM [8], where quantum effects are not dominant. In particular, the critical phase found in our model should be present in all the high- $T$  phase diagram of the QDM: indeed, the rough nature of this phase was shown to be intimately tied to the dimer hard-core constraint and not to the details of fluctuations (thermal or quantum). We note in passing that, as in the classical case, doping the QDM with monomers (static or mobile) will immediately destroy this critical phase [29]. We also think that the finite- $T$  melting of the columnar phase will proceed via a KT transition as described here everywhere in the phase diagram of the QDM (presumably, this is also the case for the melting of the plaquette phase). We note that these findings are in contrast to the finite- $T$  phase diagram of the QDM proposed by Leung and coworkers [25], who speculated that the columnar crystal would melt in two steps (with an intermediate plaquette phase), even in the classical limit.

The  $T = 0$  phase diagram of the QDM is usually accepted as this [25, 44, 45] (with the standard notation of  $t$  for the kinetic energy gained by flipping a plaquette): for large negative  $v/t$ , the system is in a columnar phase. Increasing  $v/t$ , the QDM experiences a quantum phase transition to a plaquette phase at a quite uncertain value of  $v/t$  (see discussion below). The plaquette phase ends up at the Rokhsar-Kivelson (RK) multi-

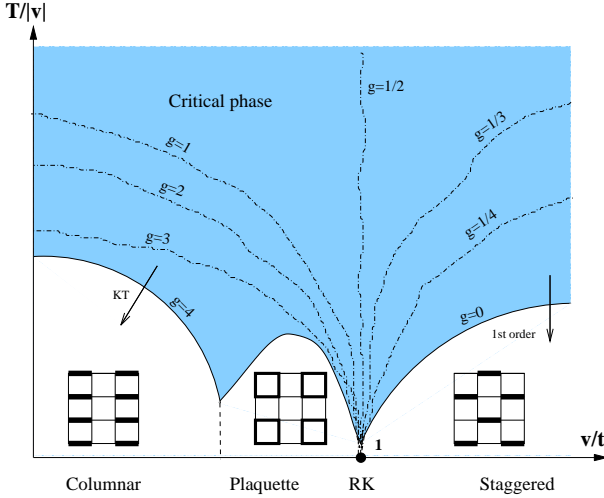


FIG. 32: (Color online) Schematic finite-temperature phase diagram of the Quantum Dimer Model on the square lattice. The different crystals (columnar, plaquette and staggered) all melt into a high temperature critical phase (denoted in blue) with algebraic correlations characterized by a Coulomb gas constant  $g$ . See text for details.

critical point  $v/t = 1$ , where the correlation functions display algebraic quasi-long range order [8]. For  $v/t > 1$ , the system is in the staggered phase.

We are now armed to connect this phase diagram to our finite- $T$  results for  $t = 0$  and draw our proposed  $(v/t, T/|v|)$  schematic phase diagram (see Fig. 32). We believe the critical phase present in the whole high- $T$  region extends down to low temperatures at the RK point. This critical phase can be parametrized by the Coulomb gas coupling constant  $g$ , and we draw lines of iso- $g$  in this region. The line  $g = 4$  denotes the boundary between the high- $T$  phase and the columnar phase (and presumably to the plaquette phase as well), corresponding to the expected KT transition. As the transition from the plaquette to the columnar phase is expected on general grounds to be first order at  $T = 0$ , we expect the transition to subsist at finite temperature. On the right hand side of the phase diagram, the rough phase will give rise to the staggered phase at low temperatures via a vanishing of the CG constant  $g \rightarrow 0$ . First results indicate that the transition is here first order [15, 46]. Finally, we conjecture that all iso- $g$  lines meet at the RK point ( $T = 0, v/t = 1$ ) (see Fig. 32), consistent with the multi-critical nature of the RK point [35]. Even though numerically difficult (see discussion below), it would be very interesting to test these predictions, especially in the vicinity of the RK point.

We now make a remark on the existence of the plaquette phase. We first note that our classical model is amenable to large-scale simulations, which is not the case of the QDM. Numerical simulations of the QDM are indeed very difficult: exact diagonalizations [25, 26] are

limited to small sizes (at most  $10 \times 10$  lattices) and even if the sign problem is absent in the QDM, Quantum Monte Carlo (QMC) calculations are notoriously hard. Some progresses have however recently been made in the Green Function QMC formulation [44, 45, 47]. These difficulties could have important consequences for the plaquette phase: indeed, we saw that plaquette correlations were important in our model and altered finite-size behavior, even on systems as large as  $160 \times 160$ . This is an indication that the plaquette phase in the QDM could as well just disappear in the thermodynamic limit. This is not so unlikely noticing that the critical point separating the columnar and plaquette phase was first reported [25] to be at  $v/t \sim -0.2$ , and then presumably around  $v/t = 0.60(5)$  when larger samples were available [44, 45]: this indicates that the plaquette phase extent actually shrinks when increasing system size.

## X. CONCLUSION

In this work, we studied a model of interacting close-packed dimers on the square lattice, where the interaction tends to align neighboring dimers. The ground-state constitutes of dimers aligned in column and is four-fold degenerate. The  $T = \infty$  point is the dimer coverings enumerating problem, and displays algebraic correlations. With the help of MC and TM simulations, we could show that the low- $T$  crystalline columnar phase leaves place to a high- $T$  critical phase, with floating decay exponents of the correlation functions. The transition takes place at  $T_c = 0.65(1)$  and is of the KT type. Via a height description of the dimer configurations, we determined the effective continuum theory with a competition between a stiffness term which favors rough height profiles (critical phase for the dimers), and a locking potential favoring heights to be locked on four particular values (forcing the dimers to align in one of the four columnar ground states). This description is equivalent to a CG of electric charges, and the locking potential is in this picture associated with the vertex operator of  $e = 4$  electric charges. This allows us to interpret all the numerical results obtained in the high- $T$  phase in terms of the CG coupling constant  $g$ , which we calculate numerically with high precision. The transition is understood in the CG language as a proliferation of  $e = 4$  electric charges. This model is probably one of the simplest and versions of a CG with floating exponents. Finally, we have established that doping the dimer model with monomers produces another critical line emanating from the KT point. There is strong numerical evidence that this line is in the universality class of the Ashkin-Teller model. The AT line terminates in a tricritical point at finite  $T_* = 0.29(2)$ , in the four-state Potts universality class. Below  $T_*$  the transition goes first-order. Besides their relevance to other classical models, the results of this work also have important implications for QDM on bipartite lattices (see Sec. IX). In particular, it indicates

that their high- $T$  phase is also critical, and we conjecture that this criticality extends down to the RK point.

### Acknowledgments

We thank C. Boutillier, E. Fradkin, C. L. Henley, W. Krauth, R. Moessner, D. Poilblanc, P. Pujol, A. Ralko and O. Syljuåsen for fruitful discussions and gratefully acknowledge Frédéric Mila and Matthias Troyer for their participation at an early stage of this work. F.A. is supported by the French ANR program. The MC simulations were performed on the Gallega cluster at SPhT using the ALPS libraries [48].

### APPENDIX A: PERTURBATIVE RENORMALIZATION GROUP FOR THE 2D SINE-GORDON MODEL

We follow here the presentation given by Levitov[49]. We write the energy of the sine-Gordon model as:

$$E = \int d^D r \left[ \frac{1}{2} (\nabla \Phi)^2 + \lambda \cos(\beta \Phi) \right]. \quad (\text{A1})$$

We introduce two cut-offs  $\Lambda$  and  $\Lambda'$  in momentum space so that the field  $\Phi$  splits into fast and slow components:

$$\Phi(k) = \Phi(k)^> + \Phi(k)^< \quad (\text{A2})$$

where  $\Phi(k)^>$  (fast) is non-zero only if  $\Lambda' \leq |k| \leq \Lambda$  and  $\Phi(k)^<$  (slow) is non-zero only if  $0 \leq |k| < \Lambda'$ .

As usual we integrate over the fast component  $\Phi^>$  to obtain a renormalized energy for the slow degrees of freedom:

$$e^{-E^{\Lambda'}(\Phi^<)} = \int \mathcal{D}[\Phi^>] e^{-E(\Phi^< + \Phi^>)}. \quad (\text{A3})$$

It is simple to see that the elastic part of the energy does not couple the slow and fast components

$$(\nabla \Phi)^2 = (\nabla \Phi^>)^2 + (\nabla \Phi^<)^2 \quad (\text{A4})$$

so that we have:

$$\begin{aligned} e^{-E^{\Lambda'}(\Phi^<)} &= e^{-\frac{1}{2} \int d^D r (\nabla \Phi^<)^2} \\ &\times \int \mathcal{D}[\Phi^>] \exp \left( -\frac{1}{2} \int d^D r (\nabla \Phi^>)^2 \right. \\ &\left. + \lambda \int d^D r \cos(\beta(\Phi^> + \Phi^<)) \right). \end{aligned} \quad (\text{A5})$$

In the limit where the cosine term can be treated perturbatively we have:

$$e^{-E^{\Lambda'}(\Phi^<) + \frac{1}{2} \int d^D r (\nabla \Phi^<)^2} \simeq \int \mathcal{D}[\Phi^>] e^{-\frac{1}{2} \int d^D r (\nabla \Phi^>)^2}$$

$$\begin{aligned} &\times \prod_r (1 + \lambda \cos(\beta(\Phi^>(r) + \Phi^<(r)))) \\ &\sim \prod_r (1 + \lambda \langle \cos(\beta(\Phi^>(r) + \Phi^<(r))) \rangle_{\Phi^>}) \\ &\sim \exp \left( \lambda \left\langle \int d^D r \cos(\beta(\Phi^>(r) + \Phi^<(r))) \right\rangle_{\Phi^>} \right), \end{aligned} \quad (\text{A6})$$

and finally:

$$\begin{aligned} E^{\Lambda'}(\Phi^<) &\simeq \frac{1}{2} \int d^D r (\nabla \Phi^<)^2 \\ &+ \lambda \left\langle \int d^D r \cos(\beta(\Phi^>(r) + \Phi^<(r))) \right\rangle_{\Phi^>} \end{aligned} \quad (\text{A7})$$

where  $\langle \dots \rangle_{\Phi^>}$  is an expectation value with respect to the (Gaussian) weight  $e^{-\frac{1}{2} \int d^D r (\nabla \Phi^>)^2}$ . This expectation value can be computed in the following way:

$$\begin{aligned} \langle \cos(\beta(\Phi^>(r) + \Phi^<(r))) \rangle_{\Phi^>} &= \\ \frac{1}{2} e^{i\beta\Phi^<(r)} \langle e^{i\beta\Phi^>(r)} \rangle_{\Phi^>} + \text{H.c.} \end{aligned} \quad (\text{A8})$$

and

$$\begin{aligned} \langle e^{i\beta\Phi^>(r)} \rangle_{\Phi^>} &\sim \int \mathcal{D}[\Phi^>] \exp \left( \int_{\Lambda' < |k| < \Lambda} \frac{d^D k}{(2\pi)^D} \{ \right. \\ &\left. - \frac{k^2}{2} \Phi_k^> \Phi_{-k}^> + i\beta \Phi_k^> e^{ikr} \} \right) \end{aligned} \quad (\text{A9})$$

The last expression is a product of Gaussian integrals. The result is:

$$\langle e^{i\beta\Phi^>(r)} \rangle_{\Phi^>} \sim \exp \left( -\frac{\beta^2}{2} \int_{\Lambda' < |k| < \Lambda} \frac{d^D k}{(2\pi)^D} \frac{1}{k^2} \right) \quad (\text{A10})$$

Combining this result with Eqs. (A7) and (A8) we get:

$$\begin{aligned} E^{\Lambda'}(\Phi^<) &\simeq \frac{1}{2} \int d^D r (\nabla \Phi^<)^2 \\ &+ \lambda^* \int d^D r \cos(\beta(\Phi^<(r))) \end{aligned} \quad (\text{A11})$$

with

$$\lambda^* = \lambda \exp \left( -\frac{\beta^2}{2} \int_{\Lambda' < |k| < \Lambda} \frac{d^D k}{(2\pi)^D} \frac{1}{k^2} \right). \quad (\text{A12})$$

If  $D = 2$  we have:

$$\int_{\Lambda' < |k| < \Lambda} \frac{d^2 k}{(2\pi)^2} \frac{1}{k^2} = \frac{1}{2\pi} \log \frac{\Lambda}{\Lambda'} \quad (\text{A13})$$

and thus

$$\lambda^* = \lambda \left( \frac{\Lambda'}{\Lambda} \right)^{\beta^2/(4\pi)}. \quad (\text{A14})$$

The elastic term is of the order of  $\Lambda^2$  for  $\Phi^>$  and of order  $\Lambda'^2$  for  $\Phi^<$ . By integrating out  $\Phi^>$ , the importance

of the elastic term has been reduced by a factor  $\left(\frac{\Lambda'}{\Lambda}\right)^2$ . The strength of the cosine potential relative to the elastic terms has thus been multiplied by

$$\left(\frac{\Lambda'}{\Lambda}\right)^{\beta^2/(4\pi)-2} \quad (\text{A15})$$

when going from  $E$  to  $E^{\Lambda'}$ . Thus, we find that the cosine term is *irrelevant* if  $\beta^2 > 8\pi$ . On the other hand, the systems goes into a locked phase when  $\beta^2 < 8\pi$ .

To make contact with Eq. (55), we take the following normalization:

$$E = \int d^D r \left[ \pi g (\nabla h)^2 + V_p \cos(2\pi p h) \right] \quad (\text{A16})$$

and we find that it is equivalent to Eq. (A1) provided  $\beta = p\sqrt{\frac{2\pi}{g}}$ . With this normalization, the cosine term is relevant when  $g > p^2/4$ . For  $p = 4$  (relevant for the square lattice dimer model), we obtain that the cosine is relevant when the stiffness  $g$  exceeds  $g_c = 4$ .

## APPENDIX B: MAPPING OF THE ONE-COMPONENT COULOMB GAS TO THE SINE-GORDON MODEL

This derivation is a slightly more detailed version of the argument presented in chapter 4 of Polyakov's book [50]. We start from a system of charges interacting with a Coulomb potential  $V(r)$ :

$$Z = \sum_N \frac{\xi^N}{N!} \sum_{\{q_a\}} \sum_{\{r_a\}} \exp \left( - \sum_{a \neq b} q_a q_b V(r_a - r_b) \right) \quad (\text{B1})$$

where  $N$  is the number of charges,  $\xi$  their fugacity,  $r_a$  ( $a = 1 \dots N$ ) their coordinates on a  $D$ -dimensional cubic lattice (with unit lattice spacing) and  $q_a \in \mathbb{Z}$  their charges.

We write the interaction in momentum space:

$$\sum_{a \neq b} q_a q_b V(r_a - r_b) = \sum_{r, r'} q(r) q(r') V(r - r') \quad (\text{B2})$$

$$= \int \frac{d^D k}{(2\pi)^D} q(k) q(-k) V(k) \quad (\text{B3})$$

where

$$q(r) = \sum_{a=1}^N q^a \delta(r - r_a) \quad (\text{B4})$$

is the charge density at  $r$  and the Coulomb potential is

$$V(k) = \frac{K}{4k^2}. \quad (\text{B5})$$

We decouple the charges (Hubbard-Stratonovich) by introducing a real scalar field  $\chi(r)$ :

$$Z = \sum_N \frac{\xi^N}{N!} \sum_{\{q_a\}} \sum_{\{r_a\}} \int \mathcal{D}[\chi(r)] \exp \left( -\frac{1}{K} \sum_r (\nabla \chi(r))^2 + i \sum_i q(r_i) \chi(r_i) \right). \quad (\text{B6})$$

Then we will perform the summation over the particle degrees of freedom: their number  $N$ , their charges  $q^a$  and locations  $r_a$ . This is just a sum over the charge density  $q(r)$ :

$$\sum_{N, \{q_a\}, \{r_a\}} \frac{1}{N!} = \sum_{\{q(r)\}}. \quad (\text{B7})$$

In the limit of small fugacity  $\xi \ll 1$ , configurations with  $|q(r)| > 1$  are exponentially suppressed, and we can keep only  $q(r) \in \{-1, 0, 1\}$ . The number of particles is thus  $N = \sum_r q(r)^2$ . We have to evaluate:

$$\sum_{q(r) \in \{-1, 0, 1\}} \xi^{\sum_r q(r)^2} e^{i \sum_r \chi(r) q(r)} \quad (\text{B8})$$

$$= \prod_r \left( \sum_{q=-1}^1 \xi^{q^2} e^{i \chi(r) q} \right) \quad (\text{B9})$$

$$= \prod_r (1 + 2\xi \cos \chi(r)) \quad (\text{B10})$$

$$\simeq \exp \left( 2\xi \sum_r \cos \chi(r) \right). \quad (\text{B11})$$

In the limit  $\xi \ll 1$ , the partition function is that of the sine-Gordon model:

$$Z \simeq \int \mathcal{D}[\chi(r)] \exp \left( -\frac{1}{K} \sum_r (\nabla \chi(r))^2 + 2\xi \sum_r \cos \chi(r) \right). \quad (\text{B12})$$

[1] J. K. Roberts, Proc. Roy. Soc. (London) A **152**, 464 (1935); R. H. Fowler and G. S. Rushbrooke, Trans. Faraday Soc. **33**, 1272 (1937).

[2] P. W. Kasteleyn, Physica **27**, 1209 (1961); H. N. V. Temperley and M. E. Fisher, Phil. Mag. **6**, 1061 (1961).  
[3] M. E. Fisher, Phys. Rev. **124**, 1664 (1961).

- [4] M. E. Fisher and J. Stephenson, Phys. Rev. **132**, 1411 (1963).
- [5] R. Kenyon, E-print math.CO/0310326 and references therein.
- [6] H. W. J. Blöte and H. J. Hilhorst, J. Phys. A **15**, L631 (1982); B. Nienhuis, H. J. Hilhorst and H . W. J. Blöte, *ibid.* **17**, 3559 (1984).
- [7] D. Huse *et al.*, Phys. Rev. Lett. **91**, 167004 (2003).
- [8] D. S. Rokhsar and S. A. Kivelson, Phys. Rev. Lett. **61**, 2376 (1988).
- [9] R. Moessner and S. L. Sondhi, Phys. Rev. Lett. **86**, 1881 (2001); G. Misguich, D. Serban and V. Pasquier, *ibid.* **89**, 137202 (2002); R. Moessner, S. L. Sondhi and E. Fradkin, Phys. Rev. B **65**, 024504 (2002); D. A. Ivanov, *ibid.* **70**, 094430 (2004).
- [10] J. M. Kosterlitz and D. J. Thouless, J. Phys. C **6**, 1181 (1973); V. L. Berezinskii, Sov. Phys. JETP **32**, 493 (1971).
- [11] B. Nienhuis, in *Phase transitions and Critical Phenomena*, edited by C. Domb and J. L. Lebowitz (Academic, London, 1987), Vol. 11.
- [12] F. Alet *et al.*, Phys. Rev. Lett. **94**, 235702 (2005)
- [13] O. J. Hellmann and E. Præstgaard, Chem. Phys. **24**, 119 (1977); D. Poland and P. K. Swaminathan, J. Chem. Phys. **71**, 1926 (1979).
- [14] J.G. Brankov, V.B. Velichkov and V.B. Priezzhev, J. Mol. Liq. **53**, 15 (1992); J.G. Brandkov and R.A. Karamikhova, Physica A **162**, 298 (1990)
- [15] C. Castelnovo *et al.*, Phys. Rev. B **73**, 144411 (2006); preprint cond-mat/0602237
- [16] D. Poilblanc *et al.*, Phys. Rev. B **74**, 014437 (2006).
- [17] S. Papanikolaou, E. Luijten and E. Fradkin, preprint cond-mat/0607316
- [18] F. Alet *et al.*, Phys. Rev. Lett. **97**, 030403 (2006).
- [19] A.W. Sandvik and R. Moessner, Phys. Rev. B **73**, 144504 (2006)
- [20] O. F. Syljuåsen and A. W. Sandvik, Phys. Rev. E **66**, 046701 (2002).
- [21] F. Alet and E. Sørensen, Phys. Rev. E **68**, 026702 (2003).
- [22] J. L. Cardy, J. Phys. A **17**, L385 (1984).
- [23] H. W. J. Blöte, J.L. Cardy, and M.P. Nightingale, Phys. Rev. Lett. **56**, 742 (1986); I. Affleck, *ibid.* **56**, 746 (1986).
- [24] J.H. Wilkinson, *The algebraic eigenvalue problem* (Oxford University Press, 1988).
- [25] P. W. Leung, K. C. Chiu and K. J. Runge, Phys. Rev. B **54**, 12938 (1996).
- [26] S. Sachdev, Phys. Rev. B **40**, 5204 (1989).
- [27] K. Binder, Z. Phys. B **43**, 119 (1981).
- [28] M. S. S. Challa, D. P. Landau and K. Binder, Phys. Rev. B **34**, 1841 (1986).
- [29] W. Krauth and R. Moessner, Phys. Rev. B **67**, 064503 (2003).
- [30] The four corners in fact have the same height.
- [31] J. Kondev and C. L. Henley, Phys. Rev. B **52**, 6628 (1995); Nucl. Phys. B **464**, 540 (1996); C. Zeng and C. L. Henley, Phys. Rev. B **55**, 14935 (1997); R. Raghavan, C. L. Henley and S. L. Arouh, J. Stat. Phys. **86**, 517 (1997).
- [32] S. Coleman, Phys. Rev. D **11**, 2088 (1975).
- [33]  $g$  is related to the stiffness constant  $K$  used in Refs. 31 by  $g = 8K/\pi$ .
- [34] By exponent, we denote the actual exponent of a charge-charge correlation function, not the scaling dimension  $X(e, m)$  of the electromagnetic operator. We have the simple relation  $\alpha(e, m) = 2X(e, m)$ .
- [35] E. Fradkin *et al.*, Phys. Rev. B **69**, 224415 (2004).
- [36] M. Levin and T. Senthil, Phys. Rev. B **70**, 220403 (2004).
- [37] J. Ashkin and E. Teller, Phys. Rev. **64**, 178 (1943).
- [38] R. J. Baxter, Phys. Rev. Lett. **26**, 832 (1971); *Exactly solved models in statistical mechanics* (Academic Press, New York, 1982).
- [39] B. Nienhuis *et al.*, Phys. Rev. Lett. **43**, 737 (1979).
- [40] If monomers (magnetic charges) were allowed, the flux would count the number of monomers on the even sublattice (magnetic charge +1) minus the number of monomers on the odd sublattice (charge -1).
- [41] S. K. Yang, Nucl. Phys. B **285**, 183 (1987); P. Di Francesco, H. Saleur and J.-B. Zuber, J. Stat. Phys **49**, 57 (1987).
- [42] C. Boutillier and B. de Tilière, preprint math.PR/0608600.
- [43] A. Luther and I. Peschel, Phys. Rev. B **12**, 3908 (1975)
- [44] O. F. Syljuåsen, Int. J. Mod. Phys. B **19**, 1973 (2005); Phys. Rev. B **71**, 020401(R) (2005)
- [45] O. F. Syljuåsen, Phys. Rev. B **73**, 245105 (2006)
- [46] The MC simulations are difficult in this case, and for  $v/t \rightarrow \infty$  a transition happening only at  $T = 0$  cannot be excluded. This would reduce the occupation of the phase diagram by the staggered phase to a simple  $T = 0$  line.
- [47] A. Ralko *et al.*, Phys. Rev. B **71**, 224109 (2005)
- [48] F. Alet *et al.*, J. Phys. Soc. Jap. Suppl. **74**, 30 (2005); M. Troyer, B. Ammon and E. Heeb, Lect. Notes Comput. Sci., **1505**, 191 (1998); see <http://alps.comp-phys.org>.
- [49] L. Levitov, MIT lectures on statistical physics; see <http://www.mit.edu/~levitov/8.334/>.
- [50] A. M. Polyakov, *Gauge fields and strings* (Harwood, 1987).